SAND--90-1525C

DE91 001226

Core Structure Heat-up and Material Relocation in a BWR Short-Term Station Blackout Accident

Rodney C. Schmidt and Sudip S. Dosanjh

Nuclear Energy Sciences and Materials Technology Department
Sandia National Laboratories, Albuquerque NM 87185

Accepted as a Thermal Hydraulics Proceedings paper for presentation at the ANS Winter Meeting in Washington, DC, November 11-16, 1990.

This work was supported by the United States Nuclear Regulatory Commission and was performed at Sandia National Laboratories, which is operated for the U.S. Department of Energy under contract number DE-AC04-76DP00789.

ABSTRACT

This paper presents an analytical and numerical analysis which evaluates the core-structure heat-up and subsequent relocation of molten core materials during a BWR short-term station blackout accident with ADS. A simplified one-dimensional approach coupled with bounding arguments is first presented to establish an estimate of the temperature differences within a BWR assembly at the point when structural material first begins to melt. This analysis leads to the conclusions that the control blade will be the first structure to melt and that at this point in time, overall temperature differences across the canister-blade region will not be more than 200 K. Next, a three-dimensional heat-transfer model of the canister-blade region within the core is presented that uses a diffusion approximation for the radiation heat transfer. This is compared to the one-dimensional analysis to establish its compatibility. Finally, the extension of the three-dimensional model to include melt relocation using a porous media type approximation is described. The results of this analysis suggest that under these conditions significant amounts of material will relocate to the core plate region and refreeze, potentially forming a significant blockage. The results also indicate that a large amount of lateral spreading of the melted blade and canister material into the fuel rod regions will occur during the melt progression process.

1. INTRODUCTION

1.1 Background

During hypothetical severe accidents in nuclear reactors, energy released by fission product decay causes the liquid coolant to boil away in the reactor core. Temperatures then increase and core structural materials eventually start melting and relocating downward. During the initial phase of melt relocation, temperatures in lower sections of the core remain low due to downward heat losses, the decrease in decay heat near the boundaries of the core, and the possible presence of some remaining liquid coolant. Large axial temperature gradients can cause the melt to refreeze and form a blockage (crust) in the lower core. As happened at the Three-Mile Island Unit 2 (TMI-2) reactor, melt can subsequently accumulate above this crust and form a molten pool. Because temperatures in the pool continue to escalate, the crust will start melting and eventually a large amount of superheated and well-mixed melt will be released into the lower plenum.

On the other hand, if the axial temperature gradient is sufficiently small, melt will not refreeze in the core. In this case, core structural materials with low melting points will liquefy first and relocate into the lower plenum with very little superheat. These two behaviors (blockage formation with the associated holdup of molten materials in the core and the continual dribbling of melt into the lower plenum) represent alternate melt progression paths that, in some sense, bound the range of possible events. The path that is relevant to a particular accident sequence will be a strong function of events preceding core melt and will depend on the type of power plant in question. However, it is evident that the core melt progression path will have a strong impact on the remainder of the accident sequence.

Of interest in this study is the possible formation of core blockages in boiling water reactors (BWRs) during short-term station blackout accidents in which the automatic depressurization system (ADS) is operational. Recent safety assessment studies[1,2] have identified this accident sequence as an important contributor to the overall plant risk of currently operating BWRs. At present, the outcome of this accident is not well understood, primarily due to uncertainty in the relevant core melt progression path. Previous analysis work using different modeling approaches has suggested two very different melt progression paths. One possiblility is that a stable blockage does not form in the reactor core; consequently, melt gradually relocates out of the core as structural materials liquefy [3]. An alternate viewpoint assumes that the accident proceeds much like TMI-2 [4]. It should not be surprizing that these two very different melt progression paths lead to very different predicted eventual outcomes for the same accident sequence.

1.2 Accident Sequence of Interest

As mentioned above, BWR short-term station blackout accidents with ADS are of interest in this study. Operation of the depressurization system will cause pressures in the vessel to fall rapidly until the vessel pressure equilibrates with the containment pressure. At this time, the coolant level will be well below the lower core support plate and temperatures in the core will be fairly uniform due to the rapid steam flow caused by the depressurization. Subsequently, core temperatures will increase due to decay heating. It will be shown in Section 2.1 that: 1) only a small amount of steam is available for oxidation because the only source of heat transfer to the liquid coolant, radiation from the bottom of the core, is small; and 2) gas phase convection is negligible at low pressures. Consequently, in the accident sequence of interest, core melt progression is insensitive to the motion of the vapor. Since reasonable core boundary and initial conditions can be prescribed, the problem can be addressed without using detailed accident codes that couple a wide range of phenomena.

1.3 Previous Studies

Numerous experiments have been conducted to study melt progression in geometries representative of pressurized water reactors (PWRs): the DF-1, DF-2 and DF-3 experiments [7] at Sandia National Laboratories; SFD [8] and LOFT [9,10] experiments at Idaho National Engineering Laboratory; CORA experiments [11] at KfK, Federal Republic of Germany; and FLHT experiments [12] at the Chalk River Reactor, Canada. In addition, detailed post-accident analyses of the TMI-2 reactor are available. This extensive data base has lead to an improved understanding of liquefaction, melt relocation, and blockage formation during hypothetical PWR accidents. This information has lead to the development of mechanistic accident analysis codes such as MELPROG[5], SCDAP[6]. These codes consider at most two dimensions and focus primarily on PWRs (although it is implicitly assumed that many of the same processes will be relevant to BWRs).

Recently, several experiments have been conducted to investigate melt progression in geometries representative of BWRs. A schematic showing a unit cell in a BWR core is shown in Fig. 1. The cross shaped control blade located in the center is composed of stainless steel and B_4C. Four square zircaloy-4 canisters containing zircaloy clad fuel rods are located around each blade. The DF-4 experiment at Sandia [13,14] as well as the recently completed CORA-16 and CORA-17 experiments at KfK (results of which are still in the process of being prepared for publication) contained fuel rods and structures representing portions of the canister and the blade. These experiments contained a wall composed of control blade material surrounded by a zircaloy box; either fourteen (DF-4) or eighteen (CORA) fuel rods were placed symmetrically around the periphery of the channel box. A significant amount of oxidation occurred during the experiments and a constant steam flow rate of about 2 gm/cm^2s was prescribed at the bottom. It will be shown in Section 2 that steam flow rates are more than two orders of magnitude smaller than this during the core heat-up phase of BWR short-term station blackout accidents with depressurization.

In all of these BWR experiments, the control blade started melting at about 1500 K due to a reaction between the steel and the B_4C. As molten blade materials relocated downward into colder regions with intact geometries, the iron in the melt interacted vigorously with the channel box walls and dissolved a considerable amount of zircaloy. This steel-B_4C-zircaloy liquid solution then flooded the fuel rod regions and dissolved a considerable amount of zircaloy cladding. Therefore, it is clear that, in BWRs, the formation of metallic blockages is dependent on highly three-dimensional flow patterns. In PWRs, the core is much more uniform and the issue of blockage formation can be considered without treating melt spreading and the interactions between melt relocating (or candling) over one structure with adjacent structures. To date, no models have been developed that treat lateral melt spreading within the core or any of the other three-dimensional effects that might be important during BWR accidents.

1.4 Present Study

This paper describes analyses that have been performed to investigate the heat-up and subsequent relocation of metallic constituents in a BWR core during one specific hypothetical accident sequence; a short-term station blackout in which the automatic depressurization system is operational. The goal here is to determine if a metallic blockage can form above the core plate using reasonable upper bounds for melt-structure friction factors and heat transfer coefficients. Also, emphasis is placed on understanding BWR-specific three-dimensional effects. The important heat transfer, melt relocation and chemical processes that were observed in the DF-4 and CORA experiments are all considered.

Sections 2 and 3 focus on heat transfer effects before melting occurs. In Section 2, a simple heat transfer analysis is used to estimate temperature differences between the fuel rods, zircaloy canister and control blade and to determine the timing of liquefaction of the various materials. This model uses approximate values for radiation heat transfer between the structures, gas-phase conduction, and conduction through the zircaloy canister; all of these heat transfer mechanisms tend to reduce the lateral temperature differences at a particular axial location.

Because blockage formation depends on axial temperature gradients near the bottom of the core, a multidimensional heat transfer model is developed in Section 3. Due to the difficulty in determining three-dimensional view factors, radiation heat transfer is treated using a diffusion approximation. This is a reasonable assumption because the analyses in Section 2 indicate that lateral temperature gradients are relatively small.

Melt relocation is modeled in Section 4 and the effects of gravity, inertia and drag are considered. The melt is allowed to spread laterally whenever materials relocating downward start accumulating in a given region. An energy equation is solved for the temperature of the melt and heat transfer to adjacent structures is modeled using a heat transfer coefficient. Molten control blade materials are allowed to interact with the canister whenever the local melt volume fraction is large enough to fill a

given fraction of the space between the blade and the box walls. A number of sensitivity analyses are also presented in Section 4.

2. SIMPLIFIED HEAT TRANSFER

It is important to note that the refreezing temperature of the molten materials that flow downward first will impact blockage formation. In the reactor core, control blade materials have the lowest melting point; liquefaction has been observed at temperatures near 1500 K due to a chemical reaction between stainless steel and B_4C. The canister and the fuel rod cladding, both of which are composed of zircaloy, have the next higher melting point (2100 K); while the UO_2 fuel has the highest melting point (3100 K). However, at a given axial level, the fuel and the cladding will be at the highest temperature due to fission product decay in the UO_2. The control blade, which has no fission heating but does have significant thermal capacitance, will be at the lowest temperature. Therefore, lateral temperature differences must be quantified in order to determine which structure melts first during the accident sequence of interest.

The goal of this section is to estimate the temperatures of the different structures and regions within a BWR assembly at the point when structural material first begins to melt. To accomplish this, we will start by establishing an upper and lower bound on the temperatures within the region of interest. Next, a series of simple one-dimensional problems will be solved in order to quantify the impact of heat transfer coupling between structures within the region. Radiation, gas-phase heat transfer, and conduction in the zircaloy canister are all considered. Finally, the effect of varying certain parameters within the one-dimensional analysis framework will be considered in order to justify a specific estimate of the temperature differences we can expect to see.

Due to the unique features of the accident sequence of interest and the specific focus of this analysis, a number of important simplifications are possible. In addition to those discussed in Section 1.2, the following assumptions are made in this analysis:

1. The effect of gas phase (steam) motion is not considered. At high gas flow velocities, convective heat transfer from the structures is important and a significant amount of energy can be transported from the core to the upper portions of the reactor vessel. In fact, these processes are very important when the depressurization system is first activated. However, once pressures in the reactor vessel and the containment equilibrate (at about 3.4 atmospheres), gas velocities are very small. Typically, the liquid water level is below the core plate at this time and further vapor flow is due to boiling in lower sections of the core only (global natural convection is not important in BWRs until the core loses geometry and vapor can flow between canisters). An upper bound for the steam flux can be obtained by balancing the maximum amount of energy that can be transported from the core to the water with the energy consumed by boiling, giving:

$$j_{st} = \frac{\sigma\, T_{bot}^4 - T_{sat}^4}{h_{fg}}, \qquad (1)$$

where

j_{st} = mass flux of the steam entering the core,
σ = Stefan-Boltzmann constant,
T_{bot} = temperature of the bottom of the core plate,
T_{sat} = saturation temperature of the water, and
h_{fg} = heat of vaporization.

At a pressure of 3.4 atmospheres the saturation temperature is 410 K and the latent heat is 2.2 MJ/kg. In Section 4 it will be shown that the maximum temperature of the core plate, before a significant amount of melt relocates downward, is on the order of 575 K. For these conditions, the above equation gives a steam flux of 0.002 kg/m^{2}s, which corresponds to a Reynolds number (Re = $j_{st}d_h/\mu$, where d_h is the hydraulic diameter of fuel rod and μ is the viscosity of the steam) of about 10^{-6}. For such small Reynolds numbers, heat transfer from the structure surfaces is dominated by gas phase conduction at low temperatures and radiation at high temperatures ($\geq$ 700 K).

Using the above value for the steam flux, the amount of energy that is transported from the core by vapor convection can also be estimated. The total amount of energy (per unit cross-sectional area) released by decay heating is on the order of 3 MW/m^2. The maximum amount of energy that the vapor can transport upward is approximately $j_{st}Cp\Delta T$. Using j_{st}= 0.002 kg/m^{2}s, Cp= 2000 J/kg•K and ΔT= 1000 K gives an energy flux due to gas motion of 0.004 MW/m^2, which is a very small fraction of the energy released. Therefore, gas phase motion has a very small effect on core heat transfer in the problem of interest.

2. Energy released by oxidation of the core structures is taken to be small compared to the decay heat . Two factors justify this assumption. The first is the very low steam flow rates involved. Oxidation of zircaloy produces 16 MJ of energy per kg of steam consumed; therefore, the steam flux given above corresponds to a release rate (per unit area) of 0.03 MW/m^2 if averaged over the entire height of the core, which is much smaller than the 3 MW/m^2 produced by fission product decay. However, the actual distance over which oxidation will occur is influenced by both the mass flow rate of the steam as well as the oxidation reaction rate - which is a strong function of temperature. At high temperatures, oxidation occurs very rapidly and the height over which all of the steam is consumed decreases significantly. Locally, the oxidation energy will equal the decay heat if all of the incoming steam is consumed over a distance of 5 cm. However, even under these conditions the combustion zone will tend to propagate downward and reduce the importance of

oxidation (that is, the energy released will not be deposited in the same 5 cm length of rods for an extended period of time).

Experiments indicate that rapid zircaloy oxidation starts at about 1780 K, when the ZrO_2 that builds up on the structures changes from a tetragonal to cubic structure (oxygen diffuses faster through the more open cubic lattice). At temperatures below this value the reaction rate is very much slower. It will be shown in the following sections that significant melt formation and relocation will occur before temperatures become high enough to allow rapid oxidation. This provides the second factor underlying the assumption that the initial relocation of molten metallic materials can be considered without treating oxidation. We also note that if it is determined in Section 4 that these materials refreeze in lower sections of the core and block the further flow of steam, oxidation can be neglected during the entire core melt progression phase of this accident sequence.

3. Axial temperature gradients are neglected in this section but will be considered in the three-dimensional model that is developed in Section 3. Such gradients are large only near the boundaries of the core due to radiation heat losses and the presence of steep gradients in decay heat generation. In the center portions of the core where melting first occurs, the decay heat profile is uniform and axial conduction can be neglected. This can be shown by comparing the characteristic distance for energy transport with the total height of the reactor core. For a given time interval, t, energy can be transferred over a distance, δ, which is given by:

$$\delta = (\alpha_{eff}\, t)^{1/2}$$

where α_{eff} = an effective thermal diffusivity. zircaloy has the highest thermal diffusivity; its thermal conductivity, density and specific heat are 30 W/m•K, 6200 kg/m^3 and 350 J/kg•K, respectively, giving a diffusivity of 10^{-5} m^2/s. Therefore, for time scales on the order of 1000 seconds, energy can be transferred over a distance of only 0.1 meters. Because this distance is small compared with the height of the core (~ 4 m), axial temperature gradients will be small wherever the decay heat is uniform over a distance appreciably greater than 0.1 m.

4. Lateral heat transfer between canisters at the axial location of interest is neglected. Since the point of interest is assumed to be the canister of maximum temperature, this assumption neglects heat losses which will occur due to surrounding canisters with lower peaking factors. These losses act to reduce the real temperatures and introduce asymmetry into the canister thermal response. Since minor asymmetries are not important in this analysis, neglecting these effects will simply yield a result which tends to slightly over-estimate the average temperature rise rate at the given location for the specified decay heat.

5. Temperature differences across the width of the canister and control blade are negligible. This implies that the Biot number, defined as:

$$Bi = \frac{h\ d}{k} \quad ,$$

is small (h is the heat transfer coefficient at the surface, d is the thickness of the structure, and k is its thermal conductivity). For high temperatures, where the effective heat transfer coefficient is largely due to radiation heat transfer, the Biot number is easily shown to be much smaller than one (Bi << 1) for both of these cases.

2.1 One-Dimensional Cases Considered

In Figure 2 a cross-section of a single canister is shown together with some specific sub-regions which have been identified with letters A though D. This figure is useful in describing a series of simple one-dimensional problems or cases which will be solved. These cases will provide the basis for estimating the temperature differences at the point of melting and also clarify the importance of various separate effects.

Case 1 - Adiabatic heat-up of a single fuel rod. This calculation provides an upper bound on the maximum temperature in the canister region. It corresponds to a calculation of region C with symmetry boundary conditions.

Case 2 - 1 fuel rod interacting with a canister and blade section. This calculation provides a lower bound on the minimum temperature in the canister region. It corresponds to a calculation of region D with symmetry boundary conditions.

Case 3 - 2 fuel rods interacting with a canister and blade section. This calculation provides an approximation to the response of the control blade side of the canister, but neglects any coupling with structures on the other side of the canister. It corresponds to a calculation of region A with symmetry boundary conditions.

Case 4 - 2 fuel rods interacting with a canister section. This calculation provides an approximation to the response of the canister region away from the control blade, but neglects any coupling with structures on the other side of the canister. It corresponds to a calculation of region B with symmetry boundary conditions.

Case 5 - Case 2 and Case 3 coupled though canister heat conduction. This calculation provides an approximation to the response of both sides of the canister assuming they are only coupled through the conduction of heat along the canister wall.

Case 6 - Case 2 and Case 3 coupled though canister heat conduction and radiation heat transfer. This calculation provides an approximation to the response of both sides of the canister

assuming they are coupled through both conduction of heat along the canister wall, as well as direct radiation heat transfer.

Case 7 - Lumped parameter analysis of entire region (infinite heat transfer rates between structures) This calculation simply provides the mean temperature response of the entire region. It must always lie between the maximum and minimum temperatures found in cases 5 and 6.

In Figure 3 the various heat transfer paths modeled in Case 6 are shown schematically. All the other cases (1-5) are subsets of this, with one or more of the heat transfer paths being removed. For example, Case 2 involves only the blade, canister 1, and rod 1, whereas Case 4 involves only rods 3 and 4 with canister 2.

2.2 Basic Equations Solved in the One-Dimensional Analysis

For each structure of interest (fuel rod, canister section, or blade section), the following simple energy equation is solved

$$M_i Cp_i \frac{dT_i}{dt} = \sum_{j=1}^{n} Q_{i-j} + Q_{decay} \quad , \tag{2}$$

where

M_i = total mass of structure i,
Cp_i ,T_i = mass average specific heat and temperature of structure i,
Q_{i-j} = heat transfer rate to neighboring structures, and
Q_{decay} = decay heat energy source (fuel rods only).

The heat transfer between any two neighboring structures "1" and "2" is approximated as follows:

$$Q_{1-2}\,(W) \approx \frac{\sigma A_{ef}}{\left(\frac{2}{\varepsilon} - 1\right)} * \left(T_{s1}^4 - T_{s2}^4 \right) + k_{steam} A_{ef} \frac{T_{s1} - T_{s2}}{\Delta x_{1-2}} \quad , \tag{3}$$

where

A_{ef} = effective surface area (set equal to the rod pitch * unit length),
ε = emissivity, set equal to 0.7,
T_{s1}, T_{s2} = surface temperatures of structures 1 and 2,
k_{steam} = thermal conductivity of steam, and
Δx_{1-2} = distance between structures 1 and 2.

As explained above, the surface temperatures of the blade and canister are assumed equal to the mean temperature of the structure. However, for the fuel rods a cladding surface temperature is approximated by the following relationship:

$$T_{clad} = T_{rod,\,avg} - f_{UO_2} * Q_{1\text{-}2} \left[\frac{1}{4\pi\, k_{UO_2}} + \frac{1}{\pi\, \rho_{UO_2}\, h_{gap}} \right] , \qquad (4)$$

where

$T_{rod,\,avg}$ = mass averaged temperature of the rod (structure 1 in this case),
f_{UO_2} = mass fraction of UO_2 in the rod (f_{UO_2} = 0.83),
$Q_{1\text{-}2}$ = heat transfer between the rod (structure 1) and its neighbor,
k_{UO_2} = thermal conductivity of the UO_2 fuel,
h_{gap} = the effective heat transfer coefficient across the fuel-clad gap, and
ρ_{UO_2} = radius of the UO_2 fuel.

In this equation the difference between the rod's mass average temperature and the cladding temperature is a function of the heat transfer at the surface and the thermal resistance of the fuel and the gap. This relationship can be derived by assuming a quadratic temperature profile within the fuel, a constant heat flux across the gap and the cladding, an adiabatic fuel-rod-centerline condition, and negligible temperature difference across the cladding. Note that this procedure allows for a different effective surface temperature to be used on each side of a given fuel rod.

In Cases 5 and 6 described in Section 2.1, there is the need to model conduction heat transfer along the canister between the two canister sections of interest. This is approximated as:

$$Q_{can1\text{-}can2}\,(W) = k_{zirc}\, A_{can} \frac{T_{can1} - T_{can2}}{\Delta x_{can1\text{-}can2}} , \qquad (5)$$

where

k_{zirc} = thermal conductivity of zircaloy,
A_{can} = cross sectional area of the canister wall (width = 0.01 m), and
$\Delta x_{can1\text{-}can2}$ = distance between the canister sections (= 0.15 m).

2.3 Solution and Results

A simple finite difference solution technique was used to solve the appropriate equations for each case of interest. Time derivatives were central differenced and a time step limitation imposed such that the maximum temperature increase for any structure during a time step was limited to one degree K. Heat transfer rates during the time step are based on time step average surface temperatures.

The initial structure temperatures were set equal to 410 K, which is the saturation temperature of steam at a pressure of 3.4 atmospheres. The geometric information for BWR cores was obtained from Ref. [15] for a standard "D-lattice" assembly. Thermal conductivity and specific heat were assumed functions of temperature and the values used were adapted from Hagrman [16,17]. The surface emissivity for the base calculations was assumed constant and set equal to 0.7 for each structure. Because the decay heat decreases to about one percent of peak power shortly after the onset of an accident and stays fixed near this value for an extended period of time, Q_{decay} was assumed constant in this analysis. For the base calculations, Q_{decay} was set equal to 310 W/(kg of UO_2), which gives a heat-up rate of about 0.8 K/s for an insulated (or adiabatic) fuel rod. This value is considerably higher than the average value of 230 W/(kg of UO_2) for a typical BWR which operates at 3580 MWth and contains 1.55×10^5 kg of UO_2.

In Figure 4 selected results from Cases 1-4, and 7 are shown. Note first the upper bound and lower bound represented by the Case 1 and Case 2 calculations. These provide a window within which the actual temperatures must fall. Also shown is the mass average mean temperature for the entire canister blade region (Case 7).

Now consider the thermal response of the blade and the canister for Case 3. For the first few hundred seconds, the Case 3 blade temperature is indistinguishable from Case 2. Gradually, the Case 3 blade temperature rises above Case 2 as the impact of energy from the second rod is felt. We also see that the canister temperatures for both Cases 3 and 4 are nearly the same during the first few hundred seconds, but the Case 3 can temperature falls below the Case 4 temperature as the heat sink effect of the blade is manifest. At about 600 seconds, the temperature difference between the blade and the can for Case 3 has reached a maximum of about 200 K. At this same point in time the Case 3 rod 2 temperature is about 350 K above the blade temperature. These large temperature differences develop initially because radiation is relatively inefficient at low temperatures. However, as time progresses and the temperatures increase, the results show how the structure temperatures gradually begin to approach each other asymptotically.

For the Case 4 results, we see how the farthest rod (see rod 3 in Fig. 3b) initially heats up at nearly the same rate as an adiabatic rod. Also, as explained above, the Case 4 canister response early on is nearly identical to the Case 3 canister. As higher temperatures are reached and radiation heat transfer becomes more effective, the canister and rod temperatures draw closer, reaching a difference of only about 15 K by 2000 sec.

Figure 5 shows temperatures in regions A and B at the time the control blade in Case 3 reaches 1500 K (the temperature at which melting was first observed in both the DF-4 [7] experiments). Also shown is the adiabatic fuel rod temperature and the average temperature. Note that the temperatures in each region are fairly uniform, the maximum temperature differences in regions A and B being 70 K and 14 K respectively. This is indicative of the strong thermal coupling at these temperatures due to radiation heat transfer. It is important to recall that the Case 3 and Case 4

calculations are completely independent, in other words, there is no heat transfer coupling between the structures in these two calculations. This of course is not representative of reality, for energy will clearly be transferred at some rate between these two regions. As a result, we would expect that the mean temperature for region A (Case 3) to be too low, and for region B (Case 4) to be too high (however, we cannot make this judgement about the temperature differences within a given region). Another way of stating this is that we expect the temperature difference between the mean temperatures in these regions (about 300 K) to be larger in these calculations than in reality.

In Figures 6 and 7, temperatures from Cases 5 and 6 are shown. In Figure 6, the effect of allowing energy to be transferred between canister regions through conduction (Case 5) can be seen. We see that without any radiation heat transfer coupling at all, this effect alone reduces the maximum temperature difference across the domain from 300 K to about 160 K. In Figure 7, the effect of both the conduction path and an approximation of the radiation coupling is illustrated. In this case the overall temperature difference is reduced to around 90 K. These figures illustrate how the addition of coupling between region A and B greatly reduces the temperature difference across the canister. However, since the actual coupling between these regions is a function of the three-dimensional geometry of the actual problem, the effective coupling employed in the one-dimensional analysis must be recognized as only a rough approximation.

To consider the impact of changing the effective coupling between the different structures as well as the value of the decay heat chosen, a sensitivity study was made by repeating the calculations for Case 6 with different values of certain parameters. In Table 1, we show the results at the time of blade melting for Cases 1-6 together with the results of re-running the Case 6 calculation with a number of different parameter changes (identified as Cases 6b through 6h). The most important of these were increasing the decay heat by 50%, decreasing the radiation heat transfer rate by 50 %, decreasing the conduction heat transfer rate through the canister by 50 %, and the result of the combination of each of the above 3 changes together. Another variation of interest was the impact of neglecting the clad-fuel temperature difference within a rod, and treating the each rod in a lumped parameter type of representation. This is shown to have a noticeable but not dominant impact on the results. We note that even in the worst case (Case 6h), the maximum temperature difference that is calculated across the region is less than 190 K.

3. THREE-DIMENSIONAL HEAT TRANSFER

A three-dimensional heat transfer model has been developed to estimate axial temperature gradients in the reactor core. Note that such gradients will impact the refreezing of downward flowing molten materials and the formation of flow blockages. The energy equation is discussed in the following section and solutions are compared to the results of the previously described one-dimensional bounding analyses in Section 3.2.

3.1 Mathematical Formulation

In Section 2 it was shown that at a given axial location, conduction and radiation are large enough to minimize lateral temperature gradients. Because temperature differences between adjacent structures are expected to be small, heat transfer can be modeled using a continuum (or porous medium) approach. Such porous media methods have previously been used by Moallemi and Viskanta [18] and by Sha et al. [19] to investigate natural convection in pressurized water reactors. In these models it is implicitly assumed that different control volumes cannot share the same fuel rod; consequently, lateral heat transfer between control volumes containing fuel rods is due to radiation and gas-phase conduction only.

Gas phase convection and oxidation are again neglected for the reasons discussed in Section 2. In addition, it is assumed that radiation heat transfer can be modeled using a diffusion approximation. This is a standard assumption in porous media problems and implies that a temperature-dependent thermal conductivity can be used in the energy equation to account for conduction as well as radiation. The primary advantage of this method is that complicated three-dimensional view factors need not be calculated.

Balancing energy stored by the solid heat capacity, diffusion and the energy released by fission product decay gives the following equation for the temperature of the solid, T_s:

$$\alpha_s \rho_s Cp_s \frac{\partial T_s}{\partial t} = \bar{\nabla} \cdot \mathbf{k_{eff}} \, \bar{\nabla} T_s + Q_s \qquad (6)$$

where

α_s = solid volume fraction,
ρ_s = solid density,
Cp_s = specific heat of the solid,
$\mathbf{k_{eff}}$ = an effective thermal conductivity, and
Q_s = decay heat.

The decay heat and the effective thermal conductivity, which is a tensor with diagonal elements only, must be specified in order to close the above equation. The decay heat is nonzero only in regions containing UO_2. At very high temperatures (above those of interest in this study), the relocation of UO_2 becomes important, and the above equation must be modified to account for the convection of decay heat. Power generation falls to approximately one percent of peak power one hour after reactor shutdown and stays fixed near this value for several days [22]. Consequently, Q_s is taken to be independent of time, although it is allowed to vary with axial position (typically, Q_s is relatively uniform in the center of the core and decreases rapidly near the boundaries). In

Figure 8 the two curves for the axial variation of Q_s chosen for the calculations to be presented here are shown . These are approximations of two typical profiles as extracted from Ref. [15].

The effective conductivity is determined from the following relation:

$$\mathbf{k_{eff}} = \alpha_g \, (k_g + 4 \, \varepsilon \, \sigma \, T^3 \, l_R) \, \mathbf{I} + \alpha_s \, k_s \, \mathbf{C} \qquad (7)$$

where

α_g = gas phase volume fraction,
k_g = gas phase conductivity,
k_s = solid phase conductivity,
ε = emissivity,
l_R = radiation path length,
$\mathbf{I}$ = identity matrix, and
$\mathbf{C}$ = connectivity tensor.

The path length l_R is the average distance radiation travels before being absorbed and is of the same order of magnitude as the distance between adjacent fuel rods. The quantity $\mathbf{I}$ is a matrix with only diagonal entries (which all equal one). The matrix $\mathbf{C}$ is a connectivity tensor with diagonal elements that determine if adjacent control volumes exchange energy due to solid phase conduction. In the downward direction, such conduction always occurs and C_{zz} equals one everywhere. In the lateral directions, C_{xx} and C_{yy} vary with position. For example, there is no lateral solid phase conduction in the fuel rod region and both C_{xx} and C_{yy} equal zero; whereas for control volumes containing portions of the canister and blade, these quantities are often nonzero to allow for conduction along these walls.

The gas is assumed to be pure steam with a thermal conductivity given by [16]:

$$k_g = 4.44 \times 10^{-6} \, T^{1.45} + 9.5 \times 10^{-5} \left(\frac{2.1668 \times 10^{-9}}{T} \, P \right)^{1.3} - 1.283668 \times 10^{-3} \qquad (8)$$

where k_g is measured in W/(m K), T is measured in K, and P is measured in N/m^2.

3.2 Results and Comparisons

The numerical mesh used in the three-dimensional calculations is illustrated in Figure 9. In the axial dimension, the mesh is refined near the bottom because of the high temperature gradients in

this region. In the horizontal plane, note that the mesh is slightly reduced near the boundary, and that both the canister and the blade are contained within these outer control volumes.

In Figure 10, axial temperature profiles for Qshape1 and l_R = (1*rod pitch) at 1800 sec into the calculation are shown. A comparison with Figure 8 shows how closely the shape of these curves follows the axial power profile specified. We also note how the temperature differences at a given axial location remain fairly constant over most of the central region of the core.

To run a calculation, an appropriate value of l_R must be specified. As explained in Section 3.1, the value of l_R should be on the order of the pitch of the fuel rod (i.e., the distance between adjacent rods). A larger value of l_R increases the effective heat transfer, reducing temperature differences, while a small value produces just the opposite. In Figures 11 and 12, the results of the one-dimensional heat transfer analysis are compared with the three-dimensional calculations for two different values of l_R. In Figure 11 the results are for l_R = (1*rod pitch). In Figure 12 the results are for l_R = (2*rod pitch). The axial location corresponds to the location of maximum temperatures (see Figure 10) and the three temperatures plotted correspond to the maximum rod temperature, and the maximum and minimum blade temperatures at that axial plane. The maximum blade temperature always occurs at the blade tip, and the minimum always occurs at the blade center. Note however that because of the numerical mesh employed, the 3-D blade temperatures are actually averages of the blade and the associated canister section immediately adjacent to the blade (see Figure 9). This is why the 3-D blade section temperatures initially increase more quickly than the 1-D calculation temperatures.

Comparison of these results show that, as expected, the smaller l_R calculation produced a greater temperature difference than the larger, yielding a total temperature difference of approximately 190 K as compared to 110 K. The 1-D blade temperature falls almost exactly at the 3-D calculation's blade tip temperature for the smaller l_R case, and falls right between the two blade temperatures for the larger l_R case. The maximum rod temperature did not change significantly with the change in l_R and compares quite well to the 1-D calculation.

Overall, these results compare well with the one-dimensional analysis and provide a basis for concluding that the approximations inherent in this approach are sufficiently valid for the purposes of this work. In the calculations to follow in Section 4 the value of l_R = (2*rod pitch) will be used.

4. MELT RELOCATION

In the previous sections it was shown that the control blade begins melting first during the accident sequence of interest. A model is presented in this section for the downward relocation of molten blade materials into colder core regions with intact structures. Of particular interest is the possible formation of a metallic blockage in the vicinity of the core support plate. A number of phenomena must be considered due to the complicated three-dimensional nature of the problem and the

possibility of chemical interactions between the melt and structures. For example, the stainless steel in the blade contains iron, which interacts vigorously with zirconium; as a consequence, molten blade materials can dissolve a significant portion of the canister wall adjacent to the blade. Once a breach forms in the can wall, melt has been observed to flood the fuel rod regions and interact with cladding.

A three-dimensional model has been developed that considers liquefaction of the core structures, melt relocation, refreezing, attack of the can walls by melt, as well as the lateral spreading of melt into the rod bundle. Heat transfer is treated using the methodology discussed in Section 3 and coupled mass, momentum and energy equations are solved for the melt. Dissolution of the zirconium in the canister and fuel cladding by molten blade materials is treated in an approximate manner. The unit cell shown in Fig. 2 is represented by a collection of control volumes, each of which contains a fuel rod or a portion of a wall as well as free space. These structures are characterized by volume fractions, species fractions, and surface-to-volume ratios.

The following simplifications are employed in addition to those discussed in Section 3:

1. Since the melt is much denser than steam and gas velocities are low (see Section 2), the presence of the vapor is assumed to have no impact on the motion of the melt. Although relocating melt will displace vapor, the detailed motion of the gas is not considered important.

2. Only an average melt velocity is considered in each control volume. Because the melt is taken to move uniformly between control volumes with a single velocity, a no-slip condition cannot be applied at solid-melt contact points. However, the flow resistance experienced by the melt due to direct contact with the structures is modeled through the use of a friction factor. Drag forces are assumed to vary linearly with the melt velocity and the proportionality constant, or friction factor, is related to the viscosity of the melt and the thickness of the melt layer.

3. Lateral spreading is initiated whenever melt fills a given control volume. It is assumed that such motion is due to hydrostatic forces.

4. As was discussed in Section 3, radiation heat transfer between adjacent structures is modeled through the use of a diffusion approximation. Radiation and conduction can then be incorporated using an effective thermal conductivity tensor whose diagonal elements vary with temperature. Results discussed in Section 3 indicate that such an approach gives reasonable results, at least until the time that liquefaction first occurs. The presence of melt in a given control volume can obviously impact radiation heat transfer between structures. In order to neglect the effect of melt on radiation heat transfer between structures, the residence time, t_{res}, of the melt in a given region must be small compared to the time scale associated with radiation heat transfer, t_{rad}. The residence time of melt in a control volume with a characteristic size of l_c is on the order of l_c/w, where w is the relocation velocity; velocities between 1 cm/s and 10 cm/s have been observed experimentally giving a maximum residence

time of 1 second in a 1 cm control volume. The time scale associated with radiation heat transfer approximately equals $l_c^2/\alpha_{eff,rad}$, where the effective thermal conductivity due to radiation heat transfer is given by

$$\alpha_{eff,rad} = \frac{\sigma T^3 l_R}{\rho Cp} .$$

Typically, $\alpha_{eff,rad}$ will be on the order of 10^{-6} m^2/s, indicating that it takes about 100 seconds for radiation heat transfer to have an impact on structure temperatures within a 1 cm control volume.

5. When the melt is in contact with an adjacent structure, energy exchange is modeled through the use of a heat transfer coefficient that depends on the solid and melt thermal conductivities, the thickness of the melt layer and the thickness of the structure (or equivalently, its surface-to-volume ratio).

6. The thermal capacity of the gas is neglected because it is small relative to the thermal capacity of the solid and the melt.

7. Molten control blade materials are allowed to interact with an adjacent canister wall whenever the melt volume fraction is greater than a critical threshold value, $\alpha_{l,cr}$. Varying this parameter did not significantly impact the results of this study.

8. Because only a limited amount of phase change information is available for B_4C-steel-zircaloy mixtures, a detailed treatment of the chemical interactions between these materials is not warranted. Instead, a simple approach is adopted that accounts for the experimentally observed attack of zircaloy by molten control blade materials. It is assumed here that molten blade materials quickly dissolve zircaloy upon contact due to an interaction between the zirconium and the iron in the steel-B_4C melt. The solubility of zirconium in the melt is estimated from a Zr-Fe phase diagram given by Hansen [20] and the properties of the liquid solution are calculated by averaging the properties of the individual components. It should be noted that the refreezing temperature of the liquid solution is very uncertain; the presence of zirconium may lower the phase change temperature by several hundred degrees. The impact of such uncertainties on the solutions is discussed further in Section 4.3.

9. Properties of individual species are taken as constants and representative values given by Hagrman [16,17] are used. Control blade materials are assumed to melt at 1500 K due to a eutectic reaction between the steel and the B_4C. The melting point of zircaloy is 2100 K and the UO_2 liquefies at 3100 K (calculations presented in this study were terminated before the temperature reached this value because only metallic relocation is of interest here).

The governing mass, momentum and energy equations (which are based on the above assumptions) are discussed in the following section. The solution technique and calculational results are described in subsequent sections.

4.1 Mathematical Formulation

Conservation of Mass. Control blade materials are treated as a single species; other species of interest include zirconium and UO_2. The following mass conservation equations, which account for melting/refreezing and melt relocation, are solved for each species k:

$$\frac{\partial}{\partial t}\left(\alpha_s\, Y_{sk}\, \rho_s\right) = -\,\Gamma_k\,, \tag{9}$$

and

$$\frac{\partial}{\partial t}\left(\alpha_l\, Y_{lk}\, \rho_k\right) + \bar{\nabla} \cdot \left(\alpha_l\, Y_{lk}\, \rho_k\, \bar{u}\right) = \Gamma_k \tag{10}$$

where

α_j = volume fraction occupied by phase j,
Y_{jk} = fraction of phase j occupied by species k,
ρ_k = density of pure species k,
$\bar{u}$ = velocity of the melt,
Γ_k = creation/depletion due to melting/refreezing,

and the subscripts l and s refer to liquid and solid, respectively. Γ_k is determined through the use of phase diagrams.

Conservation of Momentum. Three momentum equations are solved to determine the x, y and z components of the melt velocity (u, v and w, respectively). Balancing inertia, viscous drag, pressure differences, and gravity gives the following relation for the z-component of the melt velocity:

$$\alpha_l\rho_l \frac{\partial w}{\partial t} + \alpha_l\rho_l \left(u\frac{\partial w}{\partial x} + v\frac{\partial w}{\partial y} + w\frac{\partial w}{\partial z} \right) = -\left(\alpha_l\, \kappa_z\, \mu\right)w - \delta\, \alpha_l \frac{\partial P}{\partial z} - \alpha_l\rho_l\, g - w\sum_{k} \Gamma_k \tag{11}$$

where

κ = drag coefficient due to solid-melt contact,
μ = viscosity of the melt, and
δ = a coefficient that either equals one or zero depending on the flow regime.

The last term on the right hand side of the above equation accounts for changes in the momentum of the melt that are attributable to melting/refreezing. The quantity δ is set equal to zero in regions containing all three phases (solid, liquid and gas) because the motion of the gas is assumed to have no impact on melt relocation (that is, the pressure P is set equal to a constant value in these regions). However, when a flow blockage forms, melt will begin to accumulate. In regions

where melt is accumulating, w is zero and the above equation requires the addition of the pressure gradient term to balance gravity. This hydrostatic head then serves as a driving force for lateral spreading in the u and v momentum equations.

Balancing inertia, viscous drag, and pressure differences gives the following relations for the x and y direction momentum equations:

$$\alpha_l \rho_l \frac{\partial u}{\partial t} + \alpha_l \rho_l \left(u\frac{\partial u}{\partial x} + v\frac{\partial u}{\partial y} + w\frac{\partial u}{\partial z} \right) = - (\alpha_l \kappa_z \mu)u - \delta\, \alpha_l \frac{\partial P}{\partial x} - u \sum_k \Gamma_k \qquad (12)$$

and

$$\alpha_l \rho_l \frac{\partial v}{\partial t} + \alpha_l \rho_l \left(u\frac{\partial v}{\partial x} + v\frac{\partial v}{\partial y} + w\frac{\partial v}{\partial z} \right) = - (\alpha_l \kappa_z \mu)v - \delta\, \alpha_l \frac{\partial P}{\partial y} - v \sum_k \Gamma_k \qquad (13)$$

respectively. The only driving forces for lateral spreading in the x and y directions are pressure differences. Therefore, the melt will flow in the downward direction until a blockage forms and causes a flow diversion (any melt that accumulates above this blockage will result in formation of a hydrostatic head). It should be noted that melt is not allowed to flow out of the unit cell shown in Fig. 2 (that is, the velocity boundary conditions at the periphery of the cell correspond to zero flow).

The drag coefficients (κ_z, κ_x and κ_y) must be specified in order to close the above equation. The following relation, which is based on a correlation given by Bird et al. [21] for flow over vertical structures, is used to calculate flow drag in the z direction:

$$\kappa_z = \frac{3}{\tau_l^2}$$

where τ_l is the thickness of the liquid layer. The minimum value of τ_l, which results in the highest value of k_z, corresponds to a uniform layer of melt in contact with the structure, and is given by:

$$\tau_{l,min} = \frac{\alpha_l}{a_v}$$

where a_v is the solid surface area per limit volume. The thickness τ_l will be greater and κ_z will be lower if the melt flows as a rivulet over the wall (in this case, a_v in the above equation must be multiplied by a factor less than one to account for partial solid-melt contact). Note that reducing κ_z lowers the residence time of the melt in a given region and increases the distance melt can flow before refreezing. The effect of varying τ on the solutions will be discussed further in Section 4.4.

The lateral drag coefficients (κ_x and κ_y) vary with spatial position within the unit cell. When control blade materials are relocating downward and the zircaloy canister is still intact, the melt is

not allowed to spread into the fuel bundle and the appropriate lateral drag coefficient (either κ_x or κ_y, depending on the location of the control volume along the periphery of the of the can-wall) is set equal to infinity. Once a breach forms in the can-wall, melt is allowed to spread into the fuel rod region; however, because the minimum gap between fuel rods is small, the lateral friction factors in this region are an order of magnitude smaller than in the interstitial region between canisters. The effect of uncertainties in these friction factors will be discussed later in this paper.

Conservation of Energy. Balancing the enthalpy change of the solid and melt, convection, diffusion, and decay heating gives a combined (solid and melt) energy equation:

$$\frac{\partial}{\partial t} \sum_k \left[\alpha_s Y_{sk} \rho_{sk} h_{sk} + \alpha_l Y_{lk} \rho_{lk} h_{lk}\right] + \bar{\nabla} \cdot \sum_k \left[\alpha_l Y_{lk} \rho_{lk} h_{lk} \bar{u}\right]$$

$$= \bar{\nabla} \cdot \mathbf{k_{eff}} \bar{\nabla} T_s + Q_s + Q_l \qquad (14)$$

where

h_{jk} = the enthalpy of species k in phase j,

Q_s = rate of energy release (per volume) in solid, and

Q_l = rate of energy release (per volume) in the liquid.

The first term on the right hand side of the above equation accounts for diffusive transport due to conduction and radiation; the thermal conductivity tensor is determined using the methodology discussed in Section 3. When heat transfer between the melt and adjacent structures is fast, the melt and solid temperatures are equal locally and the above equation can be used to solve for the temperature. However, because melt relocation usually occurs over short time scales, the solid and melt can be at different temperatures and a second energy equation must be solved. This second equation can be expressed in terms of either solid or melt enthalpies because only two equations are independent out of the total of three (combined, solid and melt) energy equations. In this study, a melt energy equation is solved. Balancing the amount of energy stored by the melt, convection, energy generation and heat transfer to the solid gives:

$$\frac{\partial}{\partial t} \sum_k \left[\alpha_l Y_{lk} \rho_{lk} h_{lk}\right] + \bar{\nabla} \cdot \sum_k \left[\alpha_l Y_{lk} \rho_{lk} h_{lk} \bar{u}\right] = Q_l - h a_v \left[T_l - T_s\right] \qquad (15)$$

Because the liquefaction or dissolution of UO_2 is not of interest in this study and oxidation is neglected, energy release in the liquid phase can be set equal to zero.

The heat transfer coefficient must be specified to close the above equations. Energy exchange between the solid and the melt is limited by conduction across a melt layer of thickness τ_l and a

solid structure of thickness τ_s. Because these two resistances act in series, the heat transfer coefficient is given by:

$$\frac{1}{h} = \frac{\tau_l}{k_l} + \frac{\tau_s}{k_s} \tag{16}$$

It should be noted that τ_s is not an independent quantity and is related to a_v, the surface area of the solid per unit volume. Sensitivity studies conducted to quantify the effect of varying h on the solutions will be described later.

4.2 Solution Technique

The preceding set of partial differential equations were solved using standard finite-difference solution techniques. A time explicit algorithm was used with a staggered grid. Thus, principle variables are evaluated at the center of a computational cell while velocities are calculated at the edges of the cell. Convective terms are evaluated using upwind differencing while diffusion terms are calculated using central differencing.

4.3 Results and Discussion

A base case calculation is presented in the following section and the effects of uncertainties in the lateral and axial friction factors, melt-structure heat transfer coefficients, and the refreezing temperature of the B_4C-steel-zirconium liquid solution, are discussed. The effect of varying the axial power profile is described subsequently.

4.3.1 Base Case. In the calculation presented here, the Qshape1 axial power profile in Fig. 9 was used and it was assumed that the bottom of the core plate radiates to an environment at the water saturation temperature. The extent of lateral melt spreading is shown schematically in Fig. 13 at various times during the calculation; the cross-hashed region corresponds to locations where some melt has refrozen while the dark black shading represents regions where a complete blockage has formed. Note that the perspective of these figures is that of a view from the top, thus the axial location of the various regions cannot be inferred from these illustrations. Melting first occurs at the tips of the control blade after 1800 seconds elapse. This melt relocates downward into colder regions and refreezes. It is evident from Fig. 13a that a blockage begins forming near the tips of the control blade and that a small amount of material spreads into the rod bundle before 1900 seconds elapse. Note that no melting has occurred before this time in the lower left-hand corner containing the center of the control blade; this relatively cold region contains the greatest thermal mass relative to the amount of decay energy released.

By 2000 seconds the gap between the blade and the can-wall is almost completely plugged and considerable lateral spreading has occurred. Note that melt preferentially spreads into the

interstitial region between canisters due to the lower flow resistance in this direction. That is, melt is more likely to flow along the outer periphery of the canister than into the fuel rod bundle due to differences in the lateral friction factors (in the model, it is assumed that the narrow spacing between the fuel rods restricts flow in this direction and leads to a higher friction factor). As evidenced by Fig. 13d, a complete blockage has formed by 2200 seconds, well before temperatures reach the melting point of the zircaloy. This figure underscores the three-dimensional nature of the problem since a blockage forms in the center of the unit cell due to refreezing of the B_4C-steel-zirconium solution. If lateral spreading was not modeled, a blockage could form in this region only when the zircaloy cladding started melting and relocating downward.

The height of the blockage shown in Fig. 13d is not uniform with lateral position. This fact is illustrated in Fig. 14 which shows the axial extent of the blockage along a diagonal starting at the lower left-hand corner of the unit cell. In this figure, the cross-hashed region again represents locations where some melt has refrozen while in the black zone, enough melt has refrozen to form a complete blockage. It is evident that melt relocating near the control blade refreezes before reaching the core plate. This portion of the unit cell is the coldest because the blade acts as a heat sink. However, melt reaches the core plate in the center and upper right hand corner of the unit cell; in these regions, the blockage forms immediately above the core plate.

4.3.2 Lateral Friction Factors. The base case calculation was repeated with uniform lateral friction factors. Results from this calculation are shown in Fig. 15. The two solutions are virtually identical at 1900 s (see Figs. 13a and 15a) because very little lateral spreading has occurred at this time. However, significant differences arise between 2000 seconds and 2100 seconds. In the calculation with uniform lateral friction factors, the melt spreads in a fairly symmetric manner and a complete blockage does not form until about 2300 seconds. However, the axial position of blockage and the amount of melt that refreezes are not affected much by the choice of friction factors.

4.3.3 Axial Friction Factors. Figure 16 shows the effect of decreasing the axial friction by a factor of ten on the axial location of the blockage. In this case, melt reaches the vicinity of the core plate everywhere in the unit cell. Since the melt relocates faster when the axial friction factor is decreased, there is less time for heat transfer and the melt flows farther before refreezing. Although the bottom of the crust is at a lower axial position when the friction factor is decreased, the top of the crust is at the same height because refreezing starts at the same axial location. Consequently, the crust is thicker, at least near the blade region, for lower friction factors.

4.3.4 Heat Transfer Coefficient. Increasing the melt-structure heat transfer coefficient by two orders of magnitude did not significantly impact the base case calculation. This implies that local melt and structure temperatures are approximately equal locally in the base case calculation.

4.3.5 Refreezing Temperature. As mentioned earlier, iron-zirconium interactions can lower the refreezing temperature of the melt. Based on information given by Hansen [20], the lowest

possible refreezing temperature is 1200 K. Changing the refreezing temperature to this value had a major effect on the solutions. Figure 17 shows that much less melt refreezes in this case. Also, the melt reaches the core plate region everywhere in the unit cell (see Fig. 18).

4.3.6 Axial Power Shape. Using Qshape2 in Fig. 9 in place of Qshape1 did not significantly impact the solutions.

5. CONCLUSIONS

The primary goal of the one-dimensional analysis described in Section 2 was to obtain a good estimation of the temperature differences within a BWR assembly at the point when structural material first begins to melt. Based on the results of this analysis and the sensitivity to the key parameters, the following two conclusions seem warranted:

1) The control blade SS-B_4C will be the first structural material to melt and relocate.

2) At the point of initial control blade failure, the temperature difference across an assembly is estimated to be within the range of 100-200 K. Assuming the blade first begins to fail at 1500 K, this implies a maximum structure temperature within the core region of less than 1700 K when this occurs.

The three-dimensional heat-transfer and material relocation modeling described in Sections 3 and 4 was intended to provide guidance about the nature of the material relocation. Although somewhat parametric in nature, a number of key conclusions can be listed whose basis are fairly insensitive to variations in the key parameters. These include:

3) Melt is predicted to reach the core plate over a considerable portion of the unit cell. Only near the blade center is there reasonable uncertainty.

4) Significant lateral spreading of the melt into the canister region is predicted to occur.

5) After the melt reaches the core plate region, there is a strong potential for blockage formation.

Finally, we note that the parameter within this analysis that has the greatest impact on the solutions is the refreezing temperature of the melt.

6. ACKNOWLEDGEMENTS

This work was supported by the United States Nuclear Regulatory Commission and was performed at Sandia National Laboratories, which is operated for the U.S. Department of Energy under contract number DE-AC04-76DP00789.

7. REFERENCES

1. USNRC, "Severe Accident Risks: An Assessment for Five U.S. Nuclear Power Plants," Vol. 1 and 2, Second Draft for Peer Review, NUREG 1150 (June 1989)

2. A. M. Kolaczkowski et al., "Analysis of Core Damage Frequency: Peach Bottom Unit 2," Sandia National Laboratories, NUREG/CR-4550, Vol. 4, Rev. 1, SAND86-2084 (August, 1989)

3. S. A. Hodge, and L. J. Ott, "BWRSAR Calculations of Reactor Vessel Debris Pours for Peach Bottom Short Term Station Blackout," Proceedings of the 16th Water Reactor Safety Information Meeting, Gaithersburg, MD (Oct. 24-27, 1988)

4. Fauske and Associates, Inc. "Modular Accident Analysis Program (MAAP) User's Manual", IDCOR Report on Subtasks 16.2 and 16.3, Atomic Industrial Forum IDCOR Program, Bethesda, Maryland, (1987)

5. S. S. Dosanjh et al., "MELPROG-PWR/MOD1: A Two-Dimensional Mechanistic Code for Analysis of Reactor Core Melt Progression and Vessel Attack Under Severe Accident Conditions," NUREG/CR-4909, SAND88-1824 (1987)

6. C. M Allison et al., "SCDAP: A Computer Code for Analyzing Light Water Reactor Severe Core Damage," Proceedings of the International Meeting on Light Water Reactor Accident Evaluation, Cambridge, Massachusetts (1983)

7. K. O. Reil et al, "Results of the ACRR-DFR Experiments," Proceedings of the International ANS/ENS Topical Meeting on Thermal Reactor Safety, Vol. 3, San Diego, California, Feb. 26, 1986.

8. P. E. McDonald et al., "PBF Severe Fuel Damage Program: Results and Comparisons to Analysis," Proceedings of the International Meeting on Light Water Reactor Accident Evaluation, Cambridge, Massachusetts (1983)

9. L. J. Ybarrondo et al., "Examination of Loft Scaling," Proceedings of the Winter Meeting of the American Society of Mechanical Engineers, New York, NY (1974)

10. P. D. Bayless and J. M. Carpenter, "Experiment Data Report for LOFT Nuclear Small Break Experiment L3-6 and Severe Core Transient Experiment L8-1," NUREG/CR-1868, EGG-2075, Idaho National Engineering Laboratory, Idaho Falls, ID (1981)

11. S. Hagan, L. Sepold, P. Hofmann, and G. Schanz, "Out of Pile Experiments on LWR Severe Fuel Damage Behavior," Tests CORA-C and CORA-2, Kfk 4404, Kernforschungszentrum Karlsruhe, Federal Republic of Germany (1988)

12. Coolant Boilaway and Damage Progression Testing Program, Quarterly Report, NUREG/CR-4318, Vol. 2, Pacific Northwest Laboratory, Richland, WA (1985)

13. R. O. Gauntt, R. D. Gasser, L. J. Ott, "The DF-4 BWR Control Blade/Channel Box Fuel Damage Experiment," NUREG/CR-4671, SAND86-1443 (1989)

14. R. O. Gauntt, R. D. Gasser, C.P. Fryer, and J.V. Walker, "Results and Phenomena Observed from the DF-4 BWR Control Blade-Channel Box Test," Proceedings of the International ENS/ANS Conference on Thermal Reactor Safety, Avignon, France (October 2-7, 1988)

15. "BWR/6 General Description of a Boiling Water Reactor," Revised September 1980, General Electric Company, San Jose, California (1980)

16. D. L. Hagrman, G. A. Reymann, and R. E. Mason, MATPRO-Version 11 (Revision 2): A Handbook of Materials Properties for Use in the Analysis of Light Water Reactor Fuel Rod Behavior, NUREG/CR-0497 and TREE-1280, Revision 2 (August 1981)

17. D. L. Hagrman, "Materials Properties Models for Severe Core Damage Analysis," Idaho National Engineering Laboratory, EGG-CDD-5801, Interim report (May 1982)

18. M. K. Moallemi and R. Viskanta, "Coolant Recirculation in a Pressurized Water Reactor Under Loss-of-Coolant Accident Conditions," Nuclear Science and Engineering 98 , pp. 209-225 (March 1988)

19. W. T. Sha, B. T. Chao, and S. L. Soo, "Local Volume Averaged Transport Equations for Multiphase Flow in Regions Containing Distributed Solid Structures," NUREG/CR-2354, ANL-81-69, Argonne National Laboratory, Argonne, IL (December 1981).

20. M. Hansen, Constitution of Binary Alloys, Second Edition, pp. 741-743, New York: McGraw-Hill Book Company (1958)

21. R. B. Bird, W. E. Stewart, and E. N. Lightfoot, Transport Phenomena, New York: John Wiley and Sons, Inc. (1960)

22. A. V. Nero, A Guidebook to Nuclear Reactors, University of California Press (1979)

List of Tables

Table 1 Selected Results at the Time of Blade Failure for the One-Dimensional Calculations

Description	Time (sec)	T_{blade} (K)	T_{can1} (K)	T_{rod1} (K)	T_{rod2} (K)	T_{rod3} (K)	T_{rod4} (K)	T_{can2} (K)
Case 1	2533	-	-	2358	-	-	-	-
Case 2	2533	1500	1514	1536	-	-	-	-
Case 3	1995	1500	1518	1549	1570	-	-	-
Case 4	1995	-	-	-	-	1810	1804	1796
Case 5	1879	1500	1521	1543	1560	1665	1652	1635
Case 6	1837	1500	1521	1551	1579	1591	1587	1574
Case 6b - Increase decay heat by 50 %	1266	1500	1534	1580	1623	1643	1639	1619
Case 6c - Decrease radiation H.T. by 50%	1854	1500	1522	1551	1593	1610	1603	1589
Case 6d - Decrease conduction H.T. in Canister by 50%	1848	1500	1522	1554	1584	1600	1599	1587
Case 6e - Lump clad with fuel in rods	1815	1500	1521	1544	1561	1569	1569	1560
Case 6f - Eliminate gas-phase conduction through steam	1840	1500	1522	1553	1581	1593	1590	1576
Case 6g - Reduce canister thickness from 100 to 80 mm	1798	1500	1522	1551	1578	1592	1591	1580
Case 6h - Combine 6b through 6d above (worst case)	1297	1500	1535	1583	1655	1689	1687	1670

List of Figures

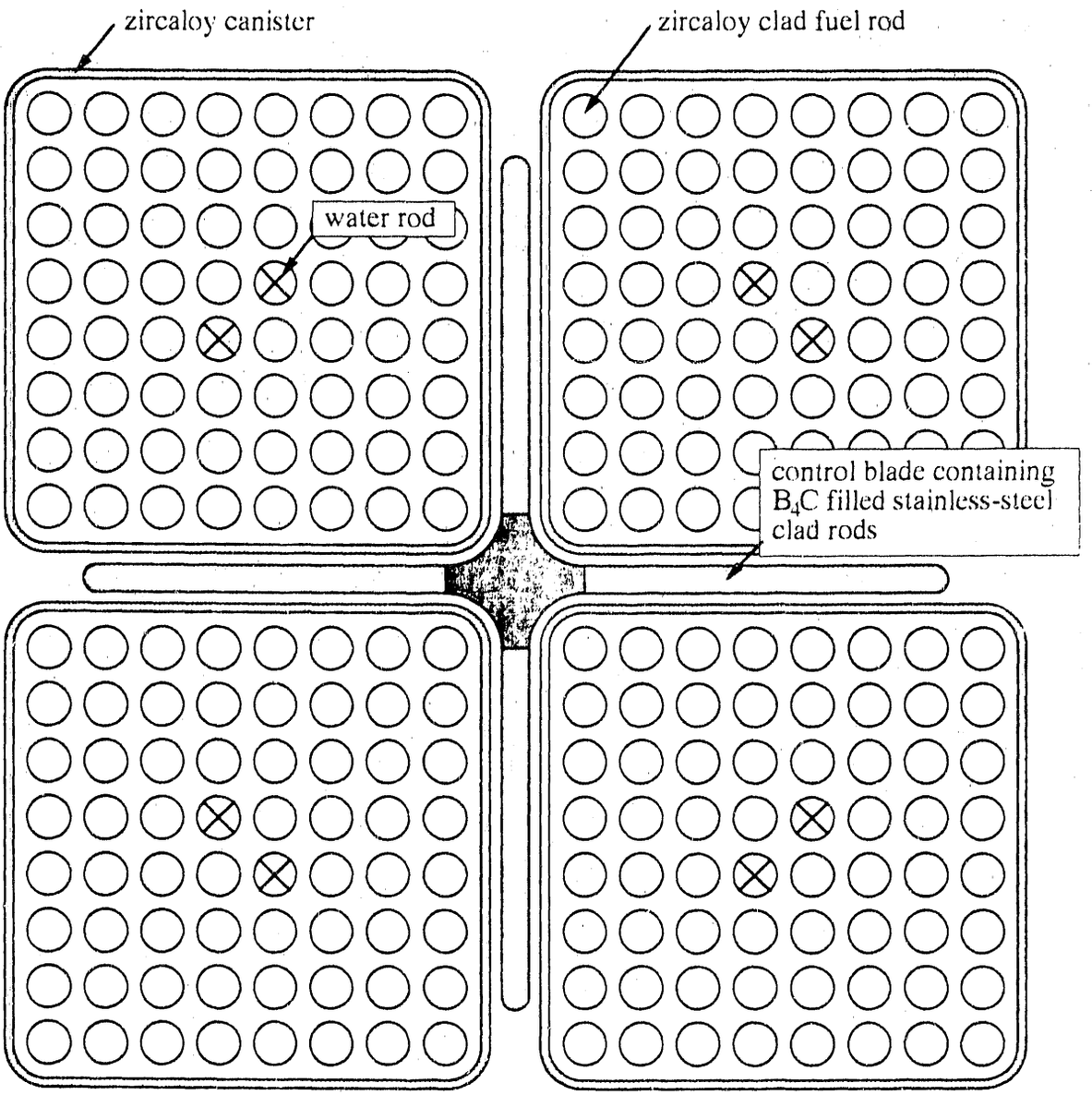

Figure 1 A cross section of a typical BWR four-bundle fuel module

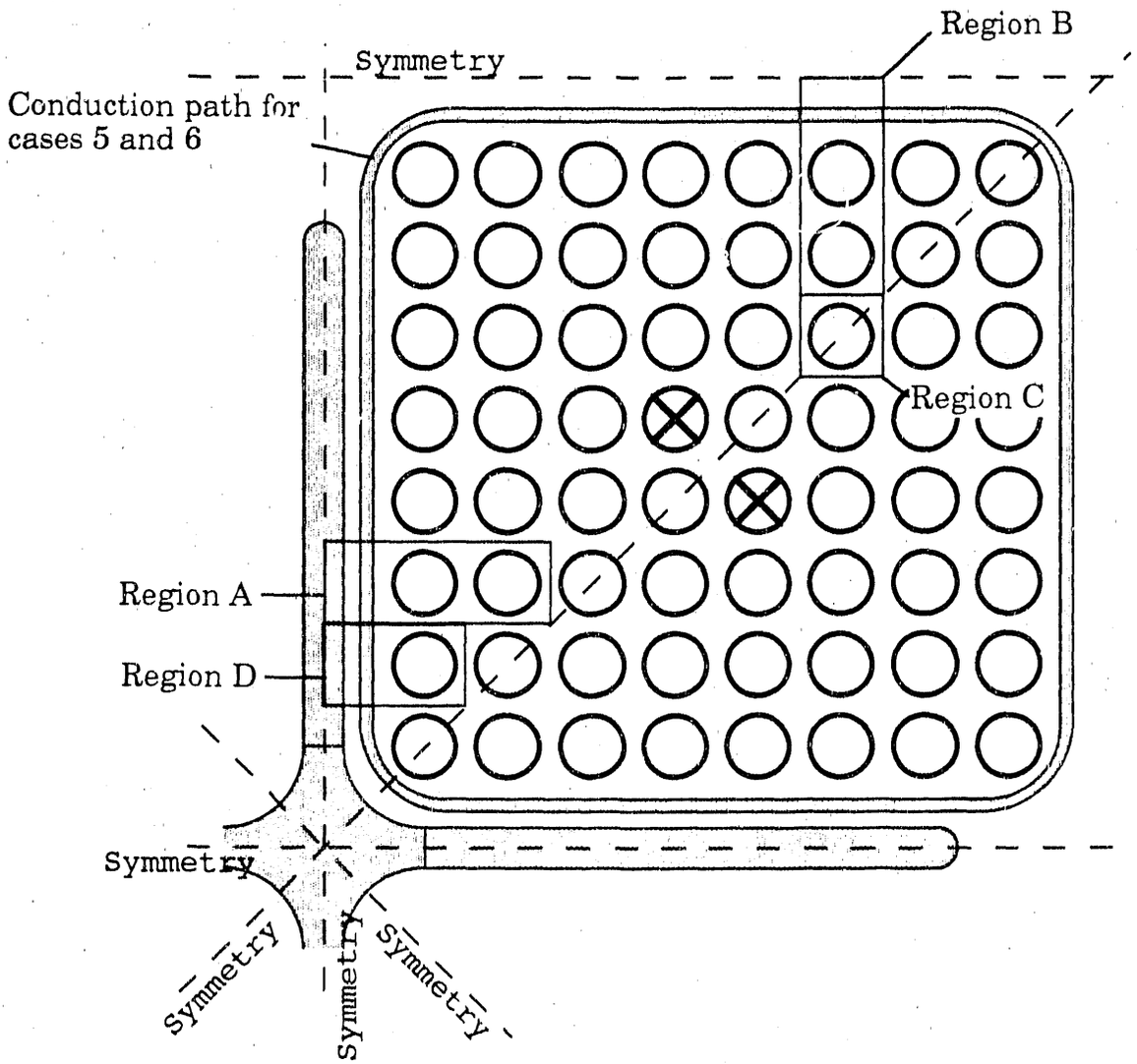

Figure 2 A BWR canister cross-section showing the sub-regions considered and the assumed symmetry

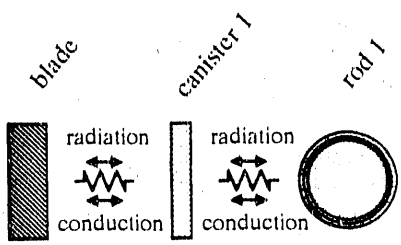

a. Case 2

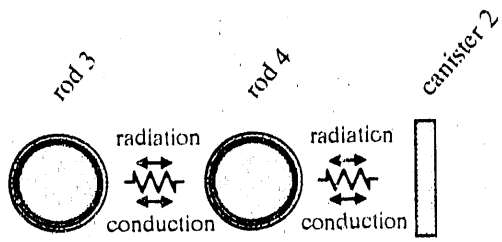

b. Case 4

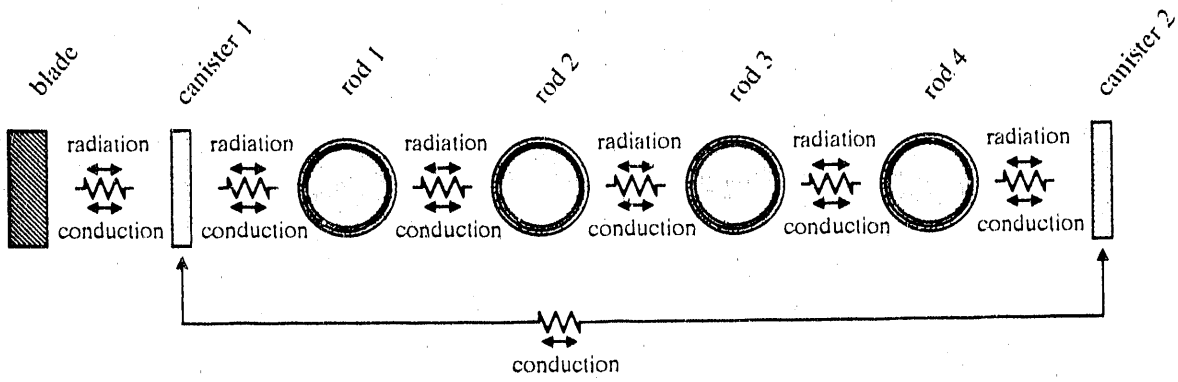

c. Case 6

Figure 3 An illustration of the heat transfer paths modeled in Cases 2, 4, and 6

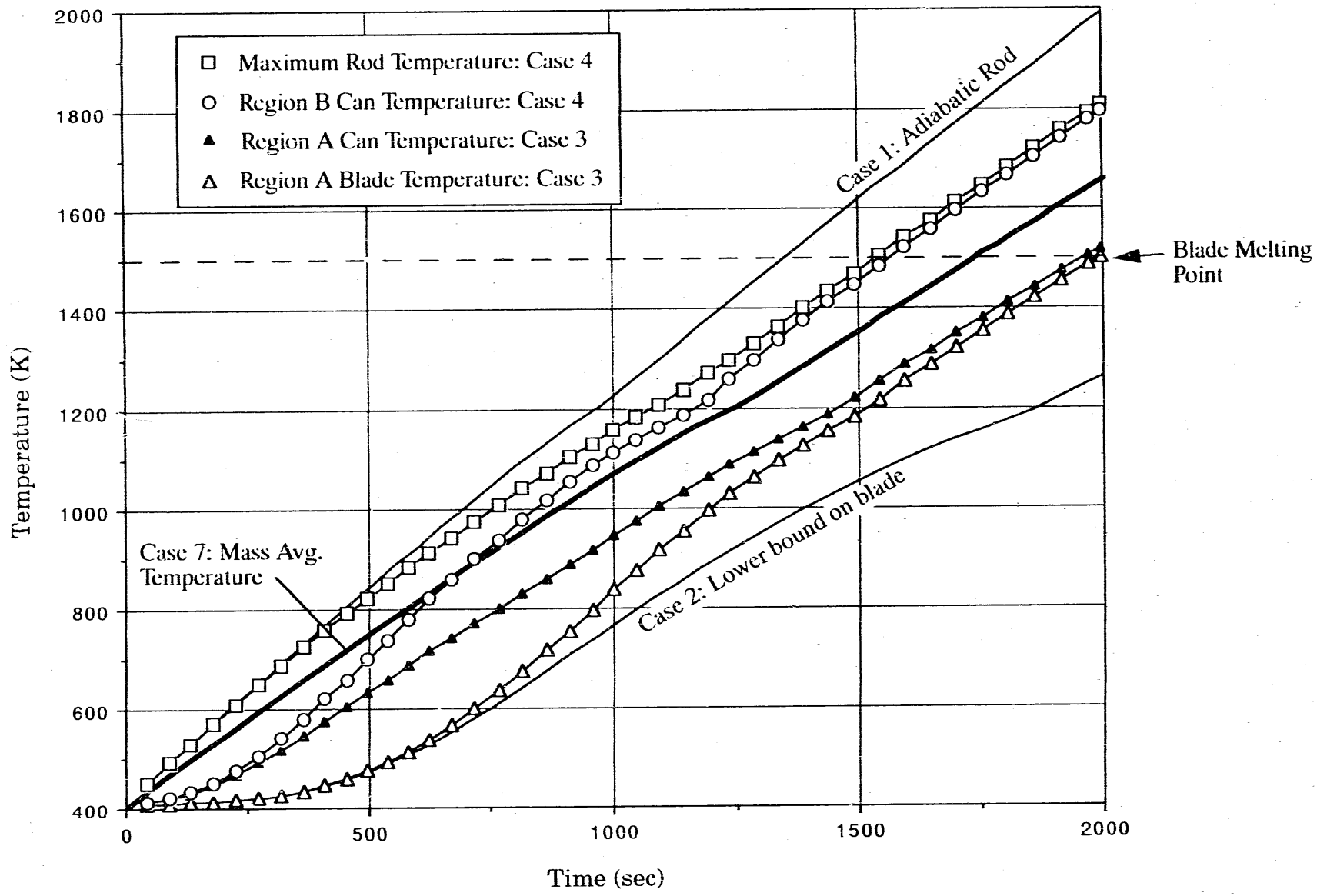

Figure 4 Some Results of the Approximate One-Dimensional Cases 3 and 4

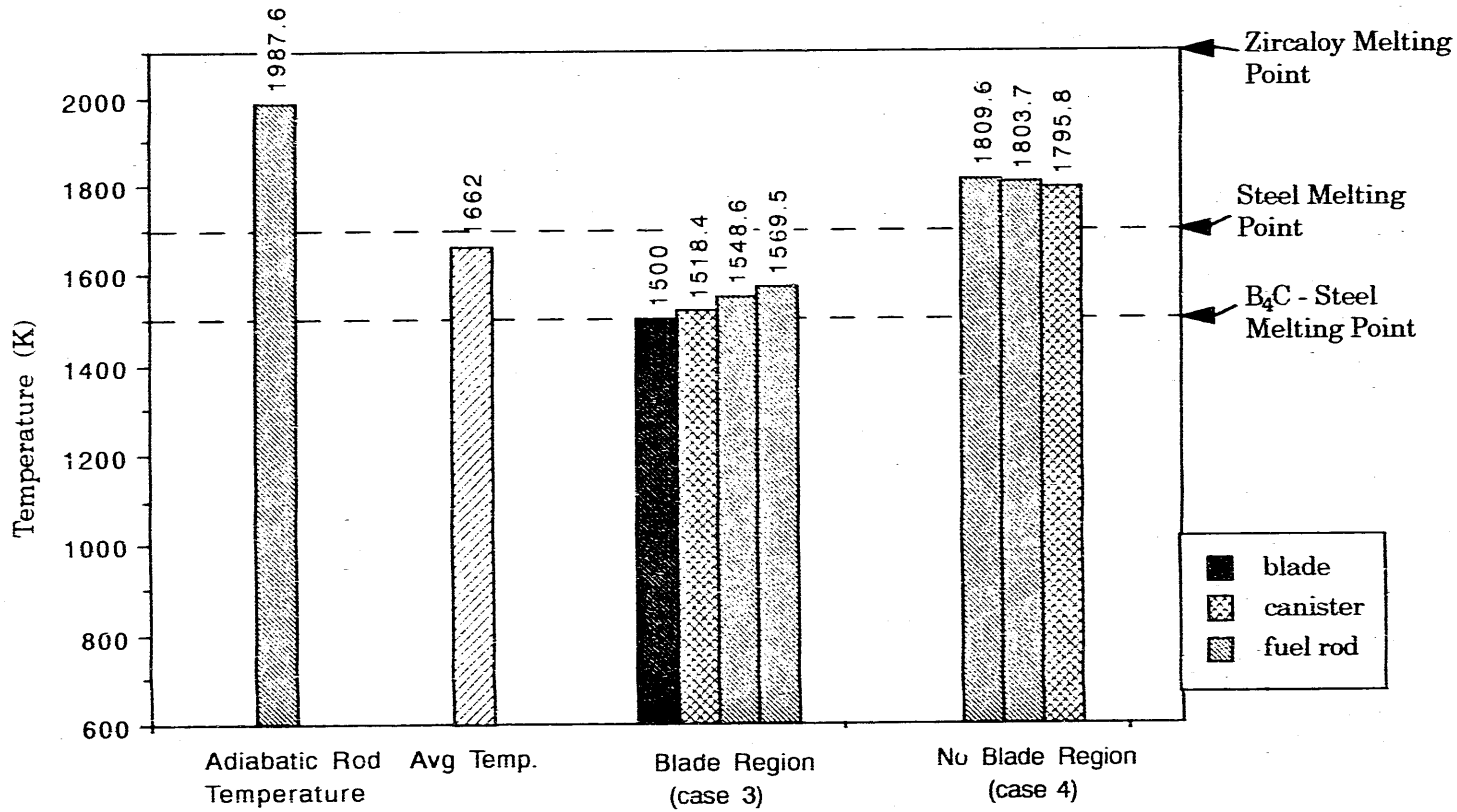

Figure 5 Structure temperatures at the point of blade failue for Cases 1, 3, 4, and 7

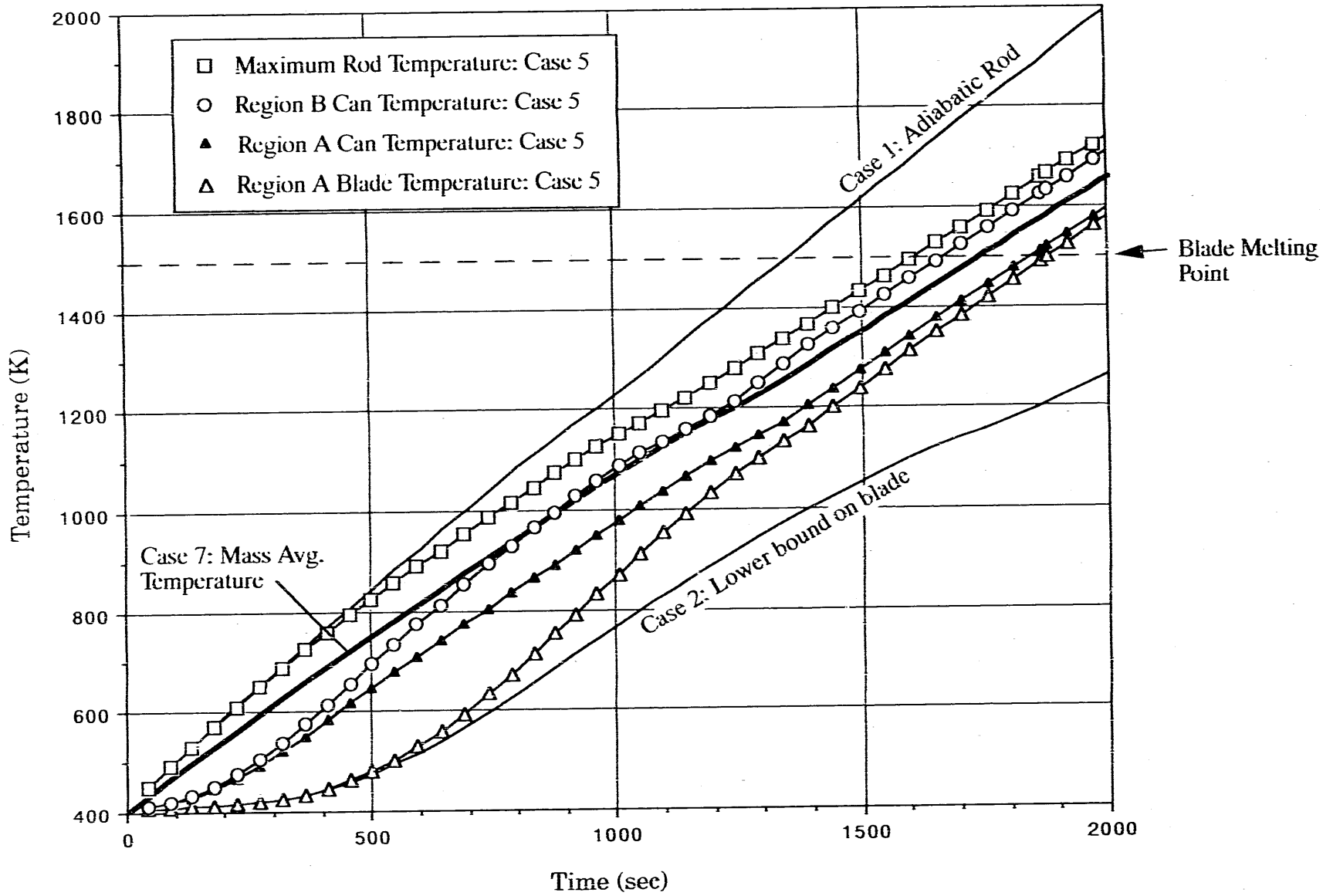

Figure 6 Some Results of the Approximate One-Dimensional Case 5

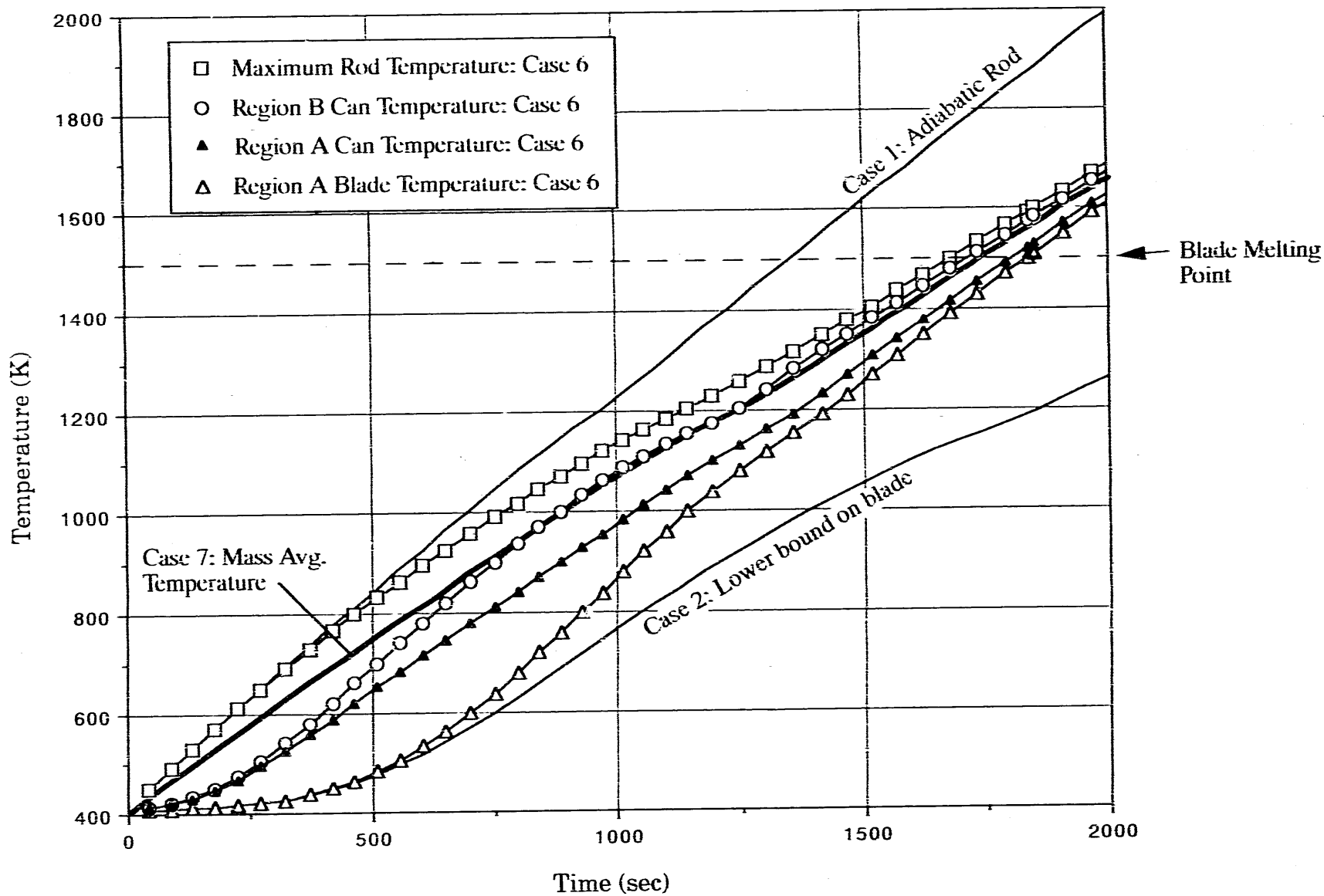

Figure 7 Some Results of the Approximate One-Dimensional Case 6

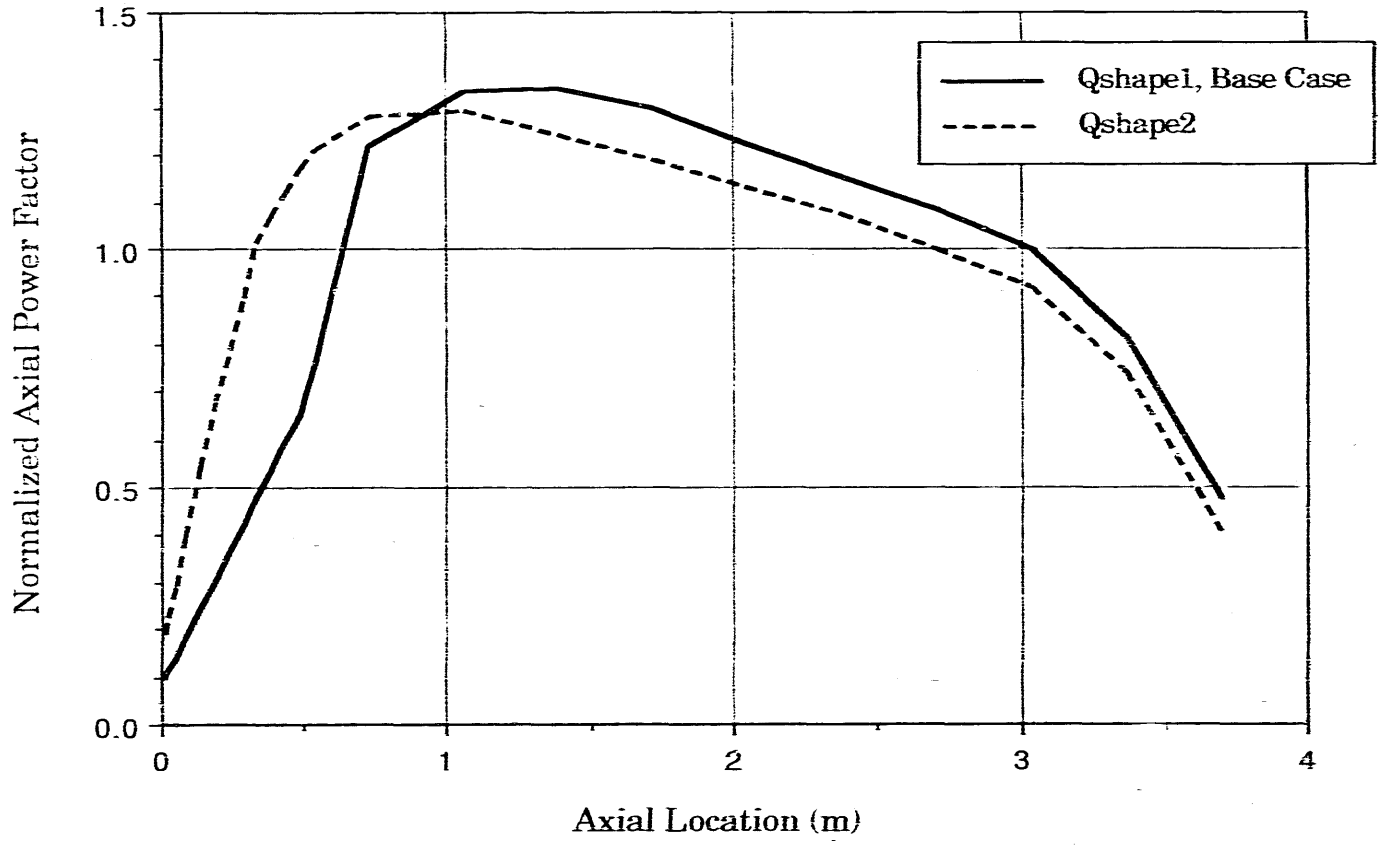

Figure 8 Axial power profiles used in the three-dimensional calculations

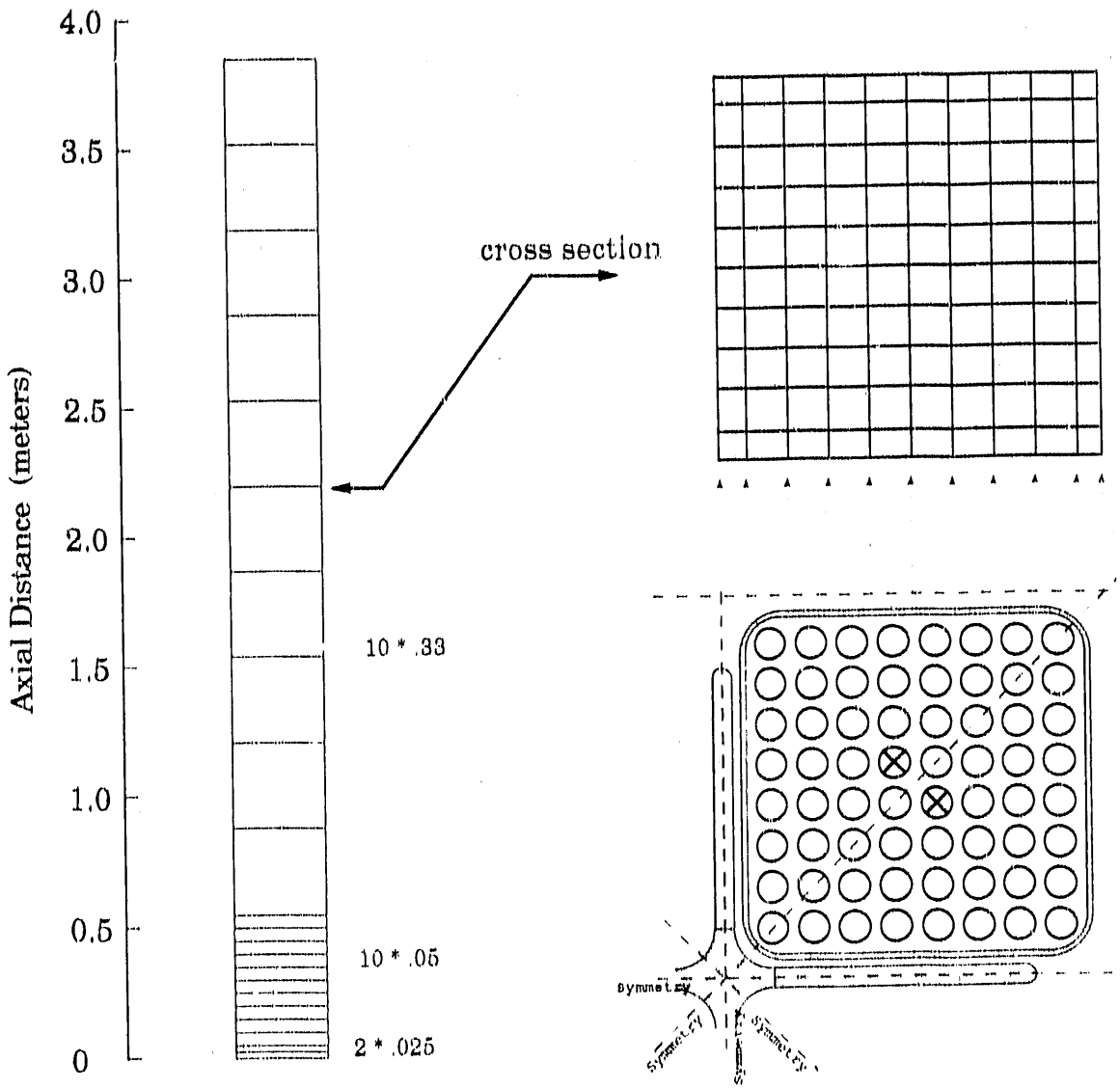

Figure 9 Numerical mesh used in the three-dimensional calculations

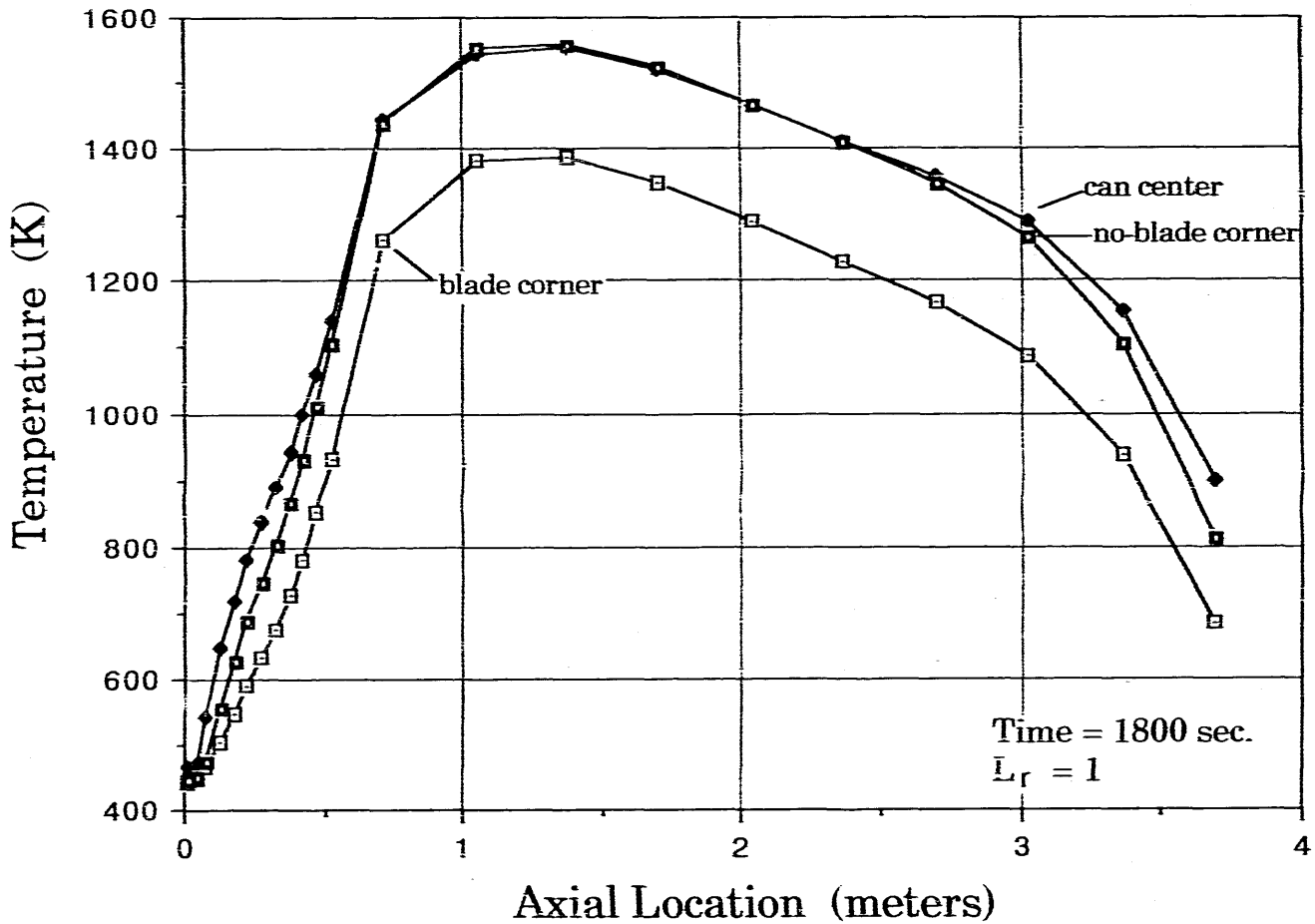

Figure 10 Axial temperature profiles at 1800 sec using Qshape1 and L_{rad}= rod pitch

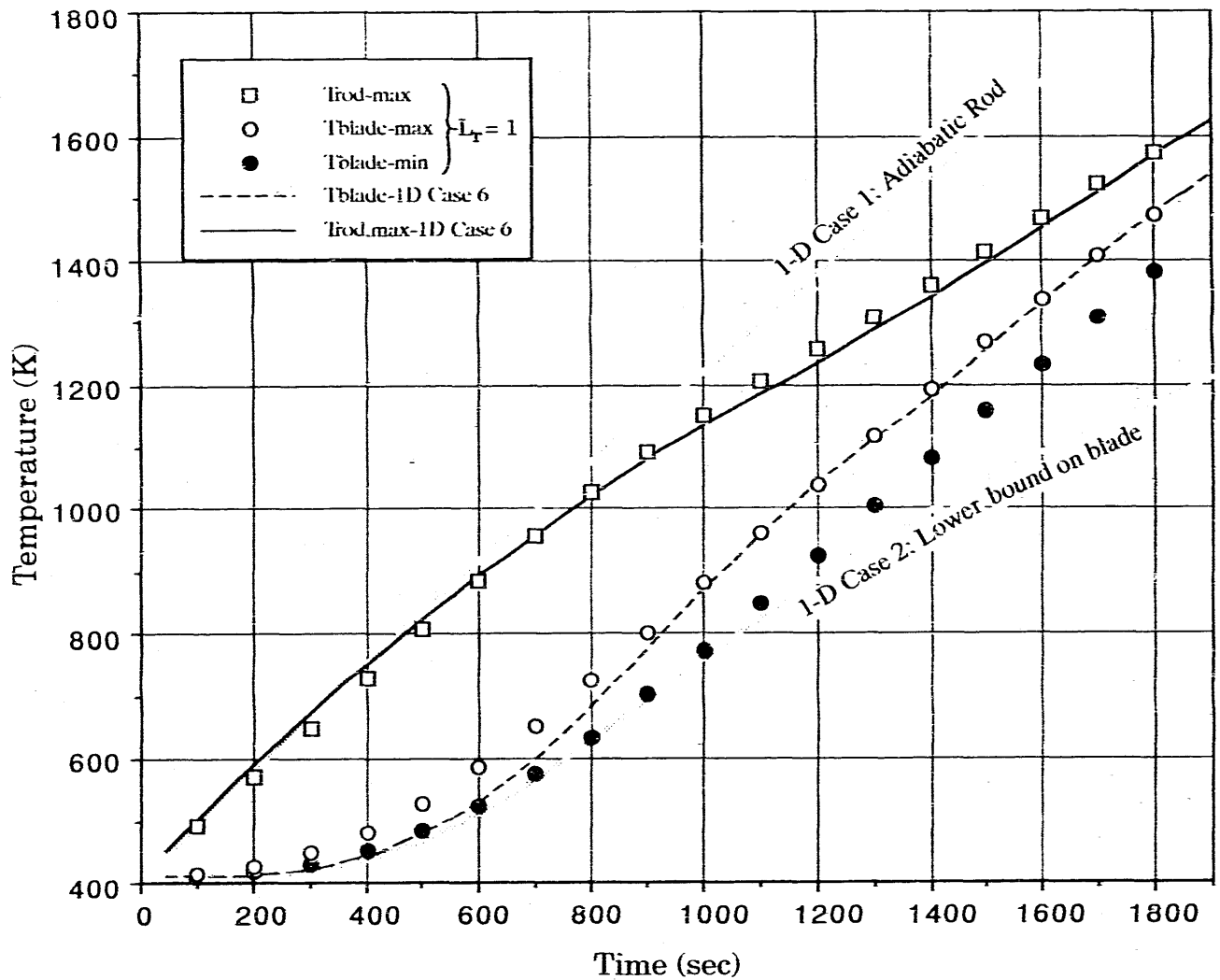

Figure 11 Comparison of the 1-D results with the 3-D model using L_{rad} = rod pitch

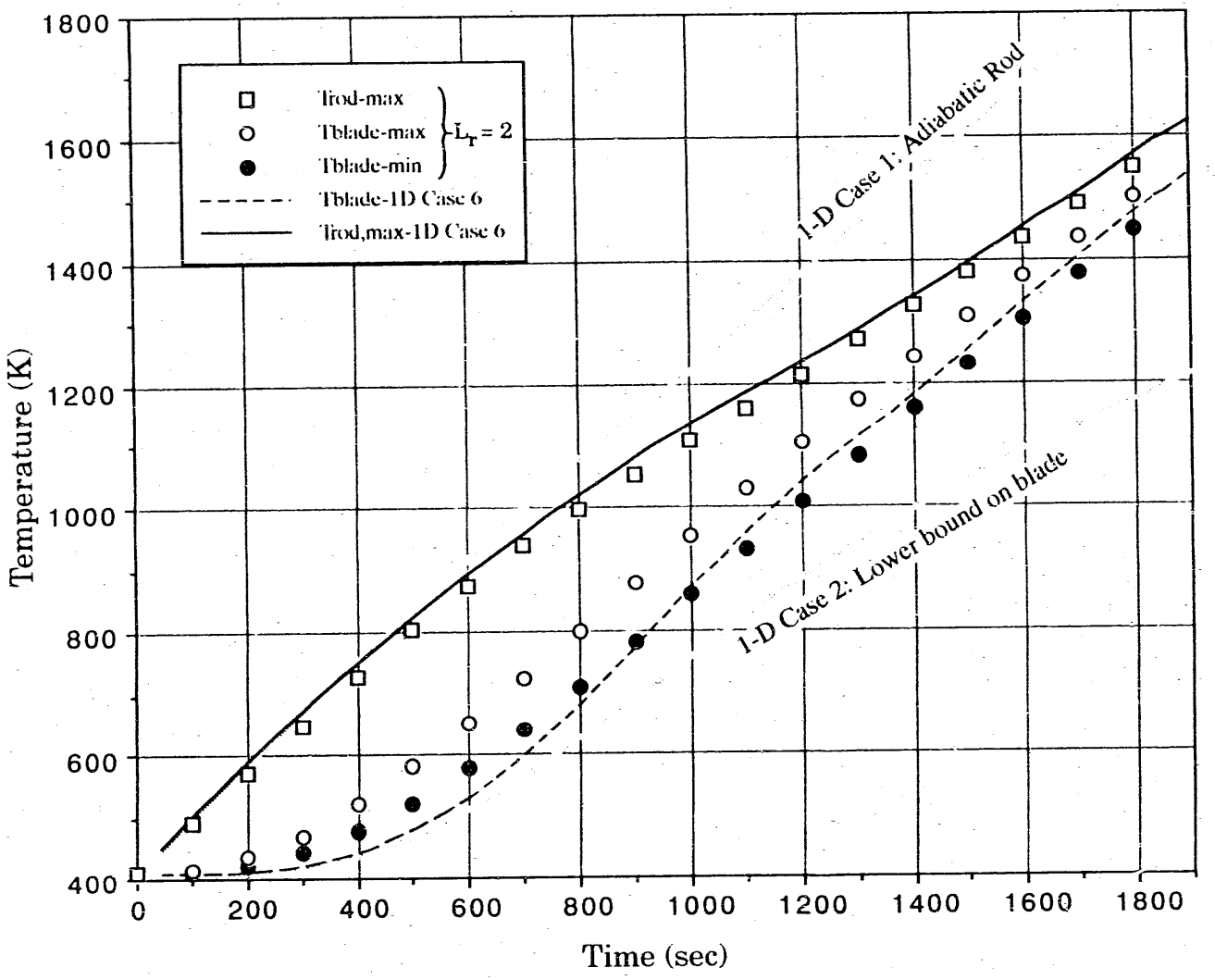

Figure 12 Comparison of the 1-D results with the 3-D model using L_{rad} = 2.*rod pitch

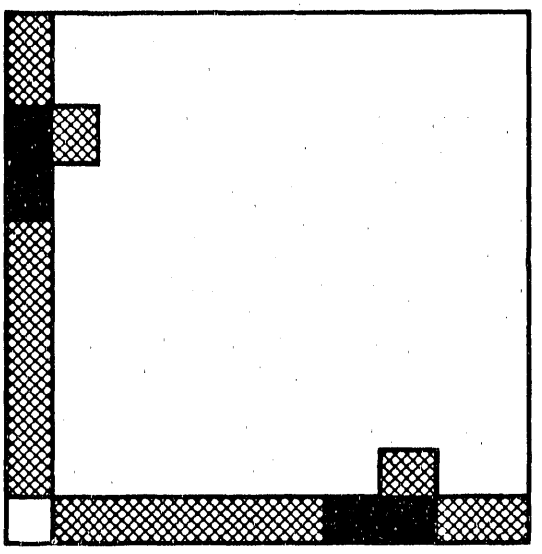

(a) 1900 sec.

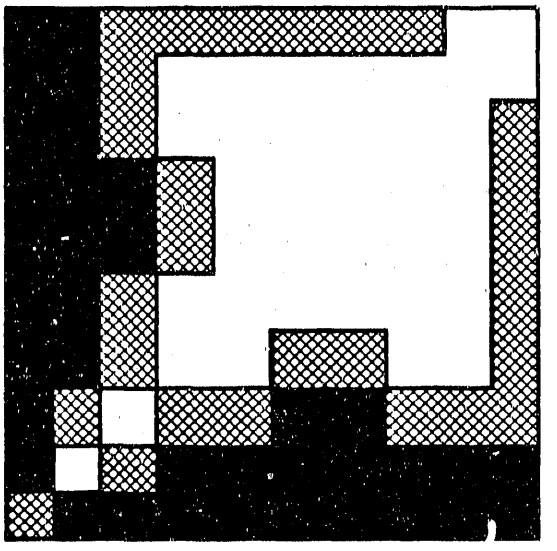

(b) 2000 sec.

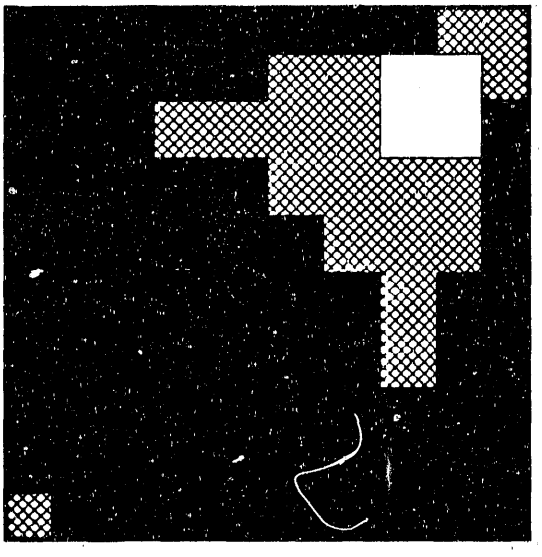

(c) 2100 sec.

(d) 2200 sec.

Figure 13 Schematic showing the lateral spreading of melt in the unit cell at various times in the base case calculation. In each figure, the control blade is in the lower, left-hand corner, the y-direction is measured toward the top of the page, and the x-direction is measured toward the edge.

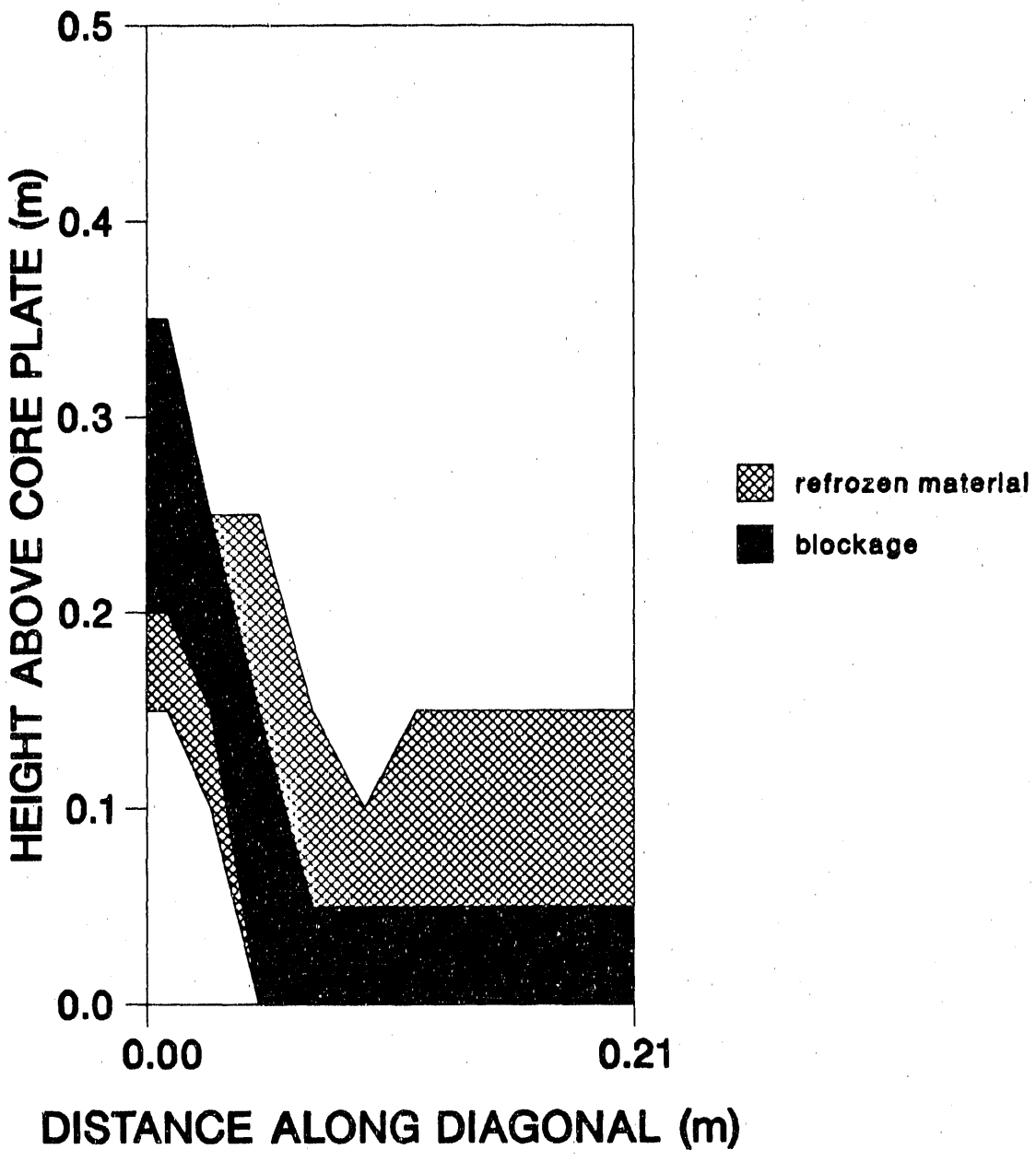

Figure 14 Blockage formation in the base case.

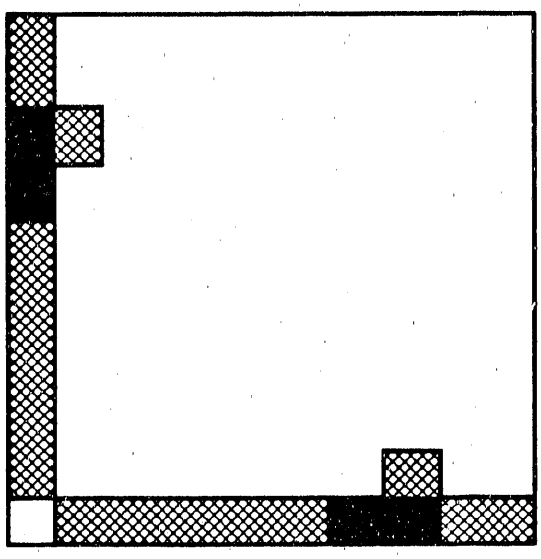

(a) 1900 sec.

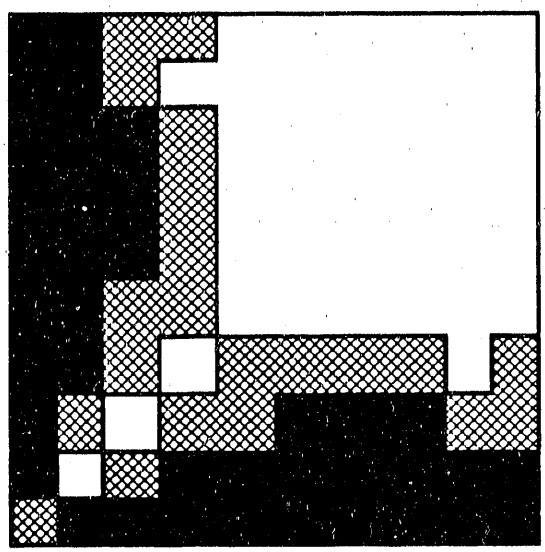

(b) 2000 sec.

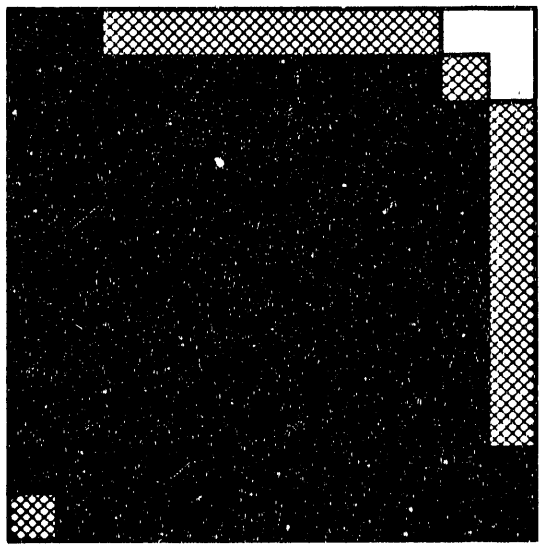

(c) 2100 sec.

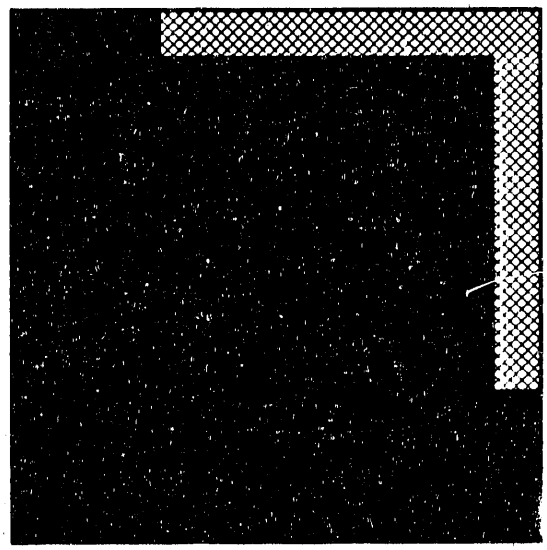

(d) 2200 sec.

Figure 15 Schematic showing the lateral spreading of melt in the unit cell at various times for a calculation with uniform lateral friction factors. In each figure, the control blade is in the lower, left-hand corner, the y-direction is measured toward the top of the page, and the x-direction is measured toward the edge.

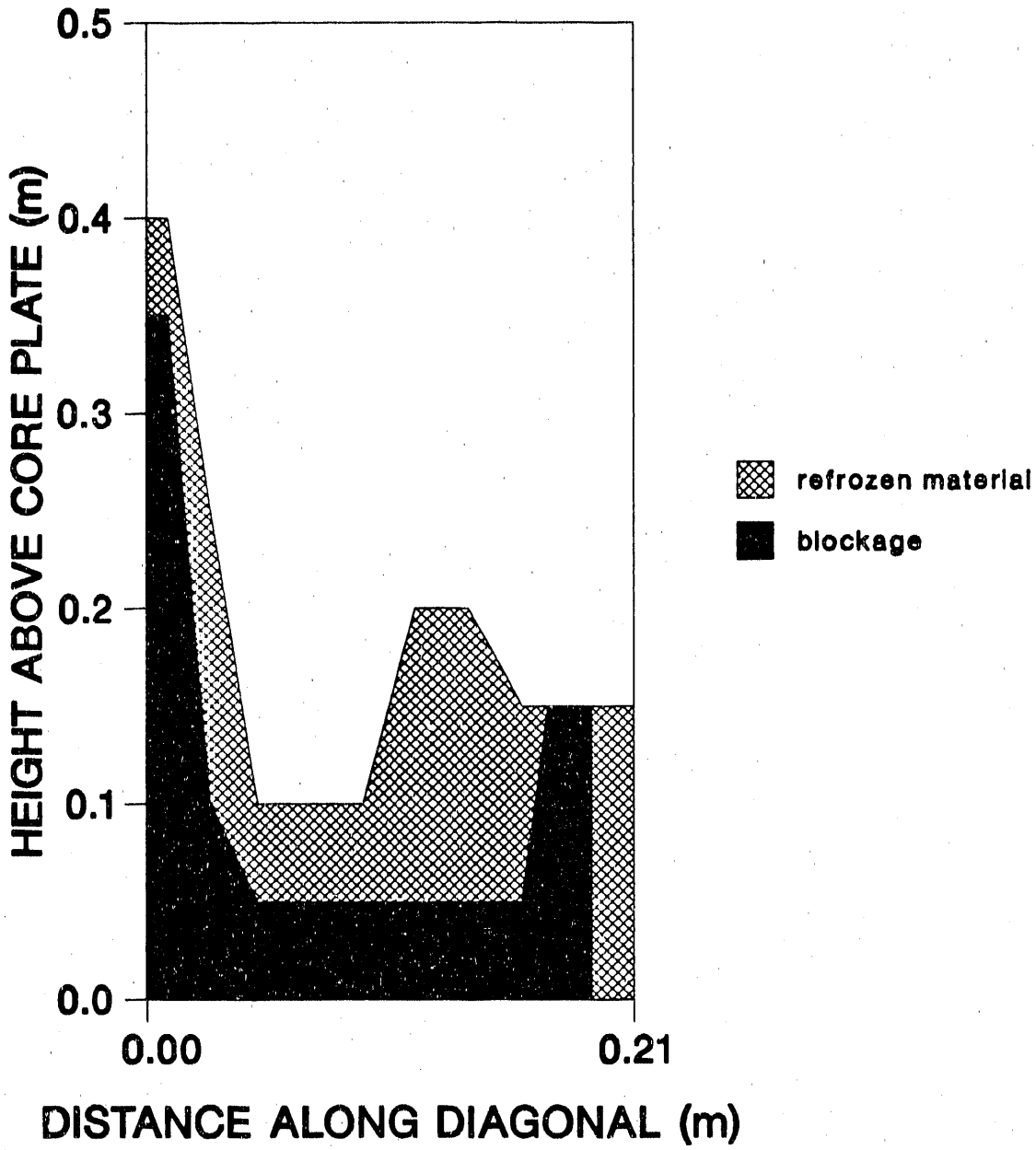

Figure 16 Blockage formation for a calculation in which the axial friction factor has been lowered by a factor of 10.

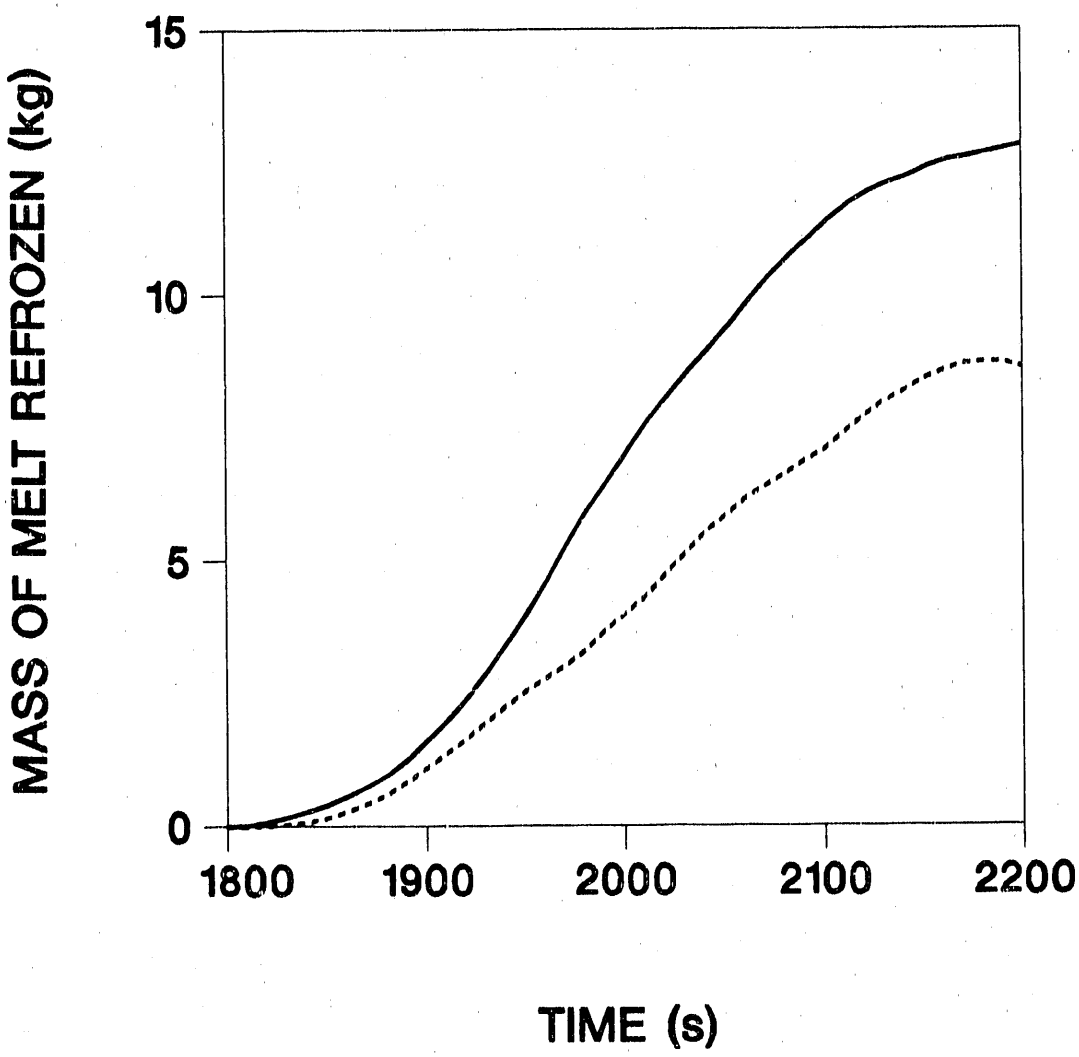

Figure 17 Mass of melt refrozen for the base case (solid line) and for a calculation in which the refreezing temperature of the blade-zirconium liquid solution has been lowered by 300 K (dashed line).

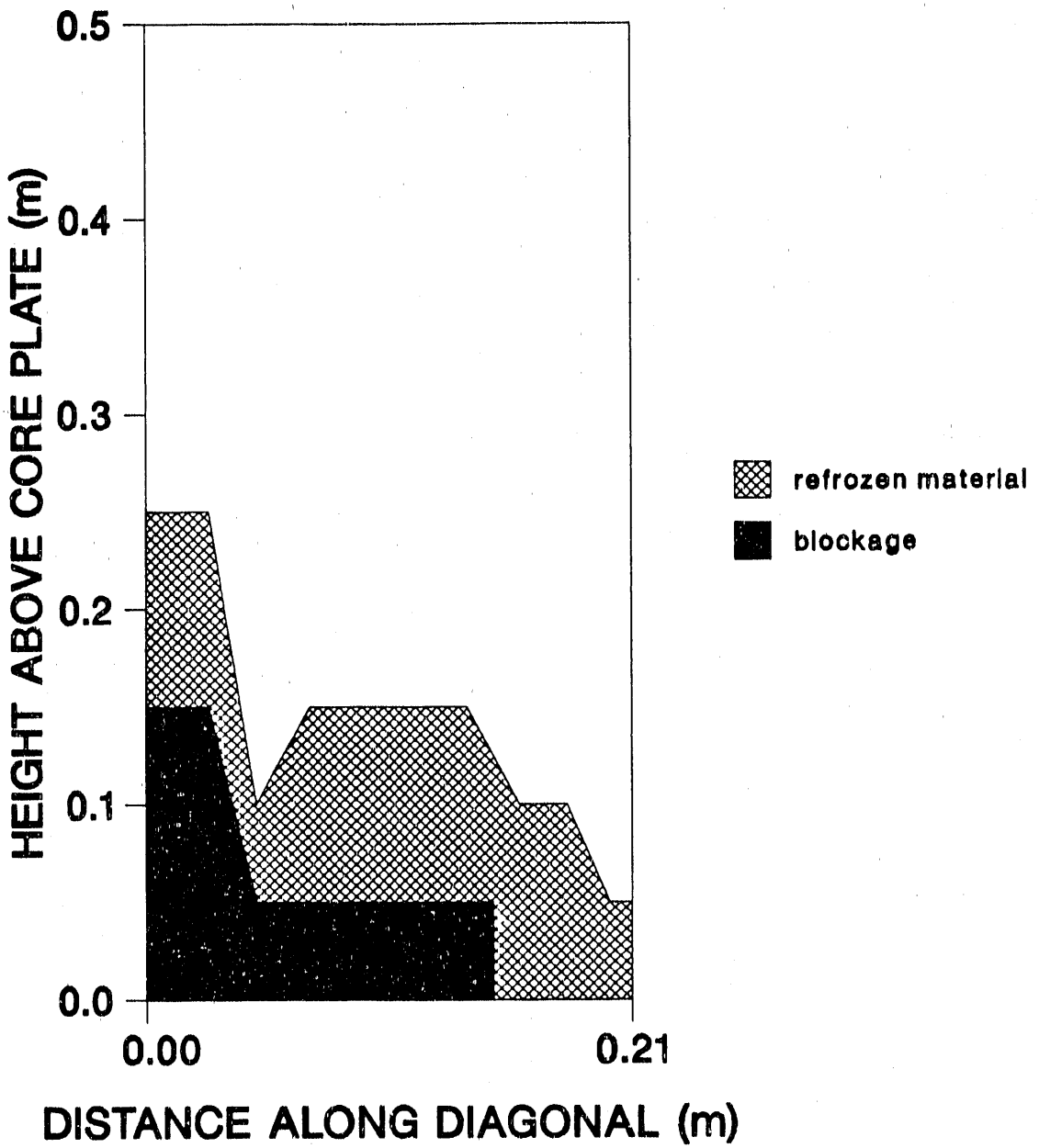

Figure 18 Blockage formation at 2200 s for a calculation in which the refreezing temperature of the blade-zirconium liquid solution has been lowered by 300 K.

END

DATE FILMED

11/08/90